Analytical Prediction of Gas Permeation through Graphene Nanopores of Varying Sizes: Understanding Transitions across Multiple Transport Regimes

Zhe Yuan[†], Rahul Prasanna Misra[†], Ananth Govind Rajan[‡], Michael S. Strano[†],
and Daniel Blankschtein[†*]

† *Department of Chemical Engineering, Massachusetts Institute of Technology, Cambridge, MA, 02139, USA*

‡ *Department of Mechanical and Aerospace Engineering, Princeton University, Princeton, NJ 08544, USA*

*E-mail: dblank@mit.edu

Abstract

Nanoporous graphene is a promising candidate material for gas separation membranes, due to its atomic thickness and low cross-membrane transport resistance. The mechanisms of gas permeation through graphene nanopores, in both the large and small pore size limits, have been reported in the literature. However, mechanistic insights into the crossover from the small pore size limit to the large pore size limit are still lacking. In this study, we develop a comprehensive theoretical framework to predict gas permeance through graphene nanopores having a wide range of diameters using analytical equations. We formulate the transport kinetics associated with the direct impingement from the bulk and with the surface diffusion from the adsorption layer on graphene, and then combine them to predict the overall gas permeation rate using a reaction network model. We also utilize molecular dynamics simulations to validate and calibrate our theoretical model. We show that the rates of both the direct impingement and the surface diffusion pathways need to be corrected using different multiplicative factors, which are functions of temperature, gas kinetic diameter, and pore diameter. Further, we find a minor spillover pathway that originates from the surface adsorption layer, but is not included in our theoretical model. Finally, we utilize the corrected model to predict the permeances of CO_2, CH_4, and Ar through graphene nanopores. We show that as the pore diameter increases, gas transport through graphene nanopores can transition from being translocation dominated (pore diameter < 0.7 nm), to surface pathway dominated (pore diameter 1–2 nm), and finally to direct pathway dominated (pore diameter > 4 nm). The various gas permeation mechanisms outlined in this study will be particularly useful for the rational design of membranes made out of two-dimensional materials like graphene for gas separation applications.

Keywords

graphene, membrane, nanopore, gas separation, molecular dynamics, gas transport.

TOC Graphics

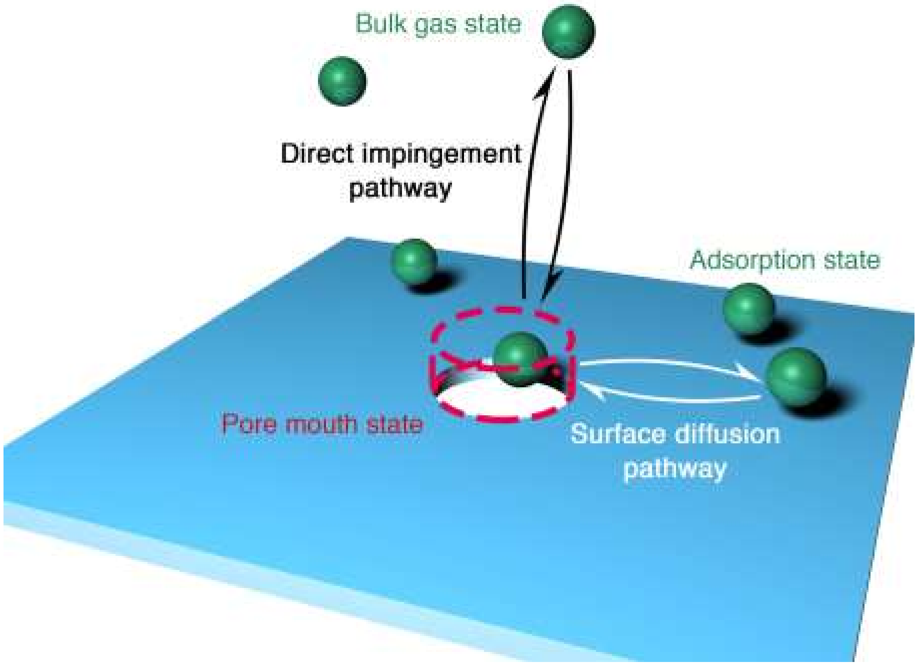

The atomic thickness of graphene endows it with tremendous potential for membrane separation.[1,2] For conventional polymeric membranes, the cross-membrane transport resistance is proportional to the membrane thickness, limiting their trans-membrane gas flux.[3] In contrast, nanoporous graphene membranes are anticipated to have extremely small molecular transport resistances and high fluxes.[3,4] The concept of membrane separation using nanoporous graphene has been demonstrated for diverse applications, such as, gas separation,[5–7] seawater desalination,[8,9] nanofiltration,[10,11] and ion separation.[12,13]

The application of permselective membranes, *i.e.*, membranes demonstrating high selectivities for gas separation processes, is currently underdeveloped, with several challenges remaining to be surmounted.[14–16] For conventional polymeric membranes, the permeability and selectivity of a given gas pair demonstrate a trade-off relationship, referred to as the Robeson upper bound.[17] This upper bound limits the overall applicability of polymeric membranes for gas separation applications. Graphene, however, has the potential to surpass the upper bound limit due to its atomic thickness and much reduced gas transport resistance.[18] In addition, the gas permeance (defined as the gas flux normalized by the driving force, *i.e.*, the pressure drop) of a nanoporous graphene membrane is linearly correlated to the areal pore density of the membrane, further boosting its potential performance.[19]

In order to achieve high selectivity for gas separation, the graphene pore diameter (D_p) should be commensurate with the collision diameter, also known as the kinetic diameter (D_m) of the gas molecules, which is typically around a few Angstroms.[20] Graphene nanopores have been experimentally created using various strategies, and the gas separation performances of the resulting nanopores have been tested in several experimental studies. Koenig *et al.* used ultraviolet-induced oxidative etching to introduce nanopores in pristine graphene.[21] A smaller nanopore (3.4 Å in diameter) exhibited pressure-normalized H_2 and CO_2 flow rates of $\sim 10^{23}$ mol s^{-1} Pa^{-1}, but the flow rates of Ar, N_2, and CH_4 were 3–4 orders of magnitude lower. A larger nanopore (4.9 Å in diameter) exhibited higher flow rates but lower separation factors among H_2, CO_2, N_2, and CH_4, while rejecting SF_6. Boutilier *et al.* created graphene nanopores with diameters below 7 Å using ion bombardment followed by oxygen plasma treatment.[22] With an appropriate amount of oxygen plasma exposure, the nanoporous graphene membrane demonstrated a gas selectivity that surpassed the Knudsen effusion selectivity, suggesting a contribution of molecular sieving resulting from nanometer-sized pores. The Knudsen effusion is also known as Graham's Law of effusion, where the rate of effusion of a gas is inversely proportional to the square root of its molecular mass.[23]

Recently, our group and Huang *et al*. observed gas separation beyond the Knudsen selectivity limit through graphene nanopores formed spontaneously during the chemical vapor deposition (CVD) of single-layer graphene, with pore diameters ranging from ~ 1 to 2.5 nm.[7,24]

These experimental datasets[7,21,22,24] span wide ranges of gas flow rates and separation factors, as well as of graphene nanopore diameters, and are likely to be governed by different gas permeation mechanisms.[25] In theory, given complete knowledge of the gas permeation mechanism, it should be possible to analytically model the mathematical relation between the gas flow rate, the pore size (and shape), and the properties of the gas species, including the molecular weight and the kinetic diameter. Such a model could then be used to fit the experimentally measured gas flow rates to predict the pore size distribution, or at least a representative pore structure. Wang *et al*. proposed two gas transport regimes, the activated regime and the steric regime, determined by the relative magnitudes of the pore diameter D_p and the gas kinetic diameter D_m.[26] Specifically, in the activated regime, D_p is smaller than, or approximately equal to D_m, and the gas molecule needs to overcome an energy barrier imposed by the pore rim atoms. Previous studies have utilized *ab initio* simulations to estimate the energy barrier for a gas molecule to translocate through graphene membranes.[3,27,28] In a recent study, we have also investigated in detail gas permeation in the activated regime using molecular dynamics (MD) simulations, and have shown that the rate of barrier crossing can be described accurately using transition state theory.[19]

On the other hand, when the pore size D_p is larger than the gas kinetic diameter D_m, the energy barrier decreases and the gas permeation is non-activated. Wang *et al*. designated this regime as "the steric regime" exhibiting an effusion-like mechanism.[26] Gas effusion through a pore occurs when the pore size is smaller than the gas mean free path, and the effusion rate of the gas depends on its rate of direct impingement from the bulk.[5] However, various studies have demonstrated the significance of another pathway: surface diffusion.[25,29–31] The carbon atoms in graphene exert attractive van der Waals forces on the gas molecules, which in turn, get adsorbed on the graphene surface, thereby forming an adsorption layer. The adsorbed gas molecules then diffuse to the pore region and subsequently permeate to the other side of the membrane. This surface diffusion pathway occurs simultaneously with the direct impingement pathway, and can be important, or even dominant, when the local density of gas molecules adsorbed on the graphene basal plane is high.[29]

In spite of the research efforts mentioned above, a comprehensive mechanism that unifies the different gas transport regimes has not yet been advanced. More specifically, the following challenges remain. First, the direct impingement pathway, the surface diffusion pathway, and the activated permeation have not been integrated into a general analytical equation. Second, the governing equations of the direct impingement and surface diffusion pathways, although recognized, have not been refined and validated using simulation tools. With the above two points in mind, in this study, we propose to formulate a model that incorporates all the different transport regimes, including deriving a general analytical expression to predict the gas permeance through different sizes of graphene nanopores based on the model. In addition, we utilize MD simulations to refine the expression derived from the model, and discuss the origins of these refinements. Based on the model, we are able to study the contributions, from the direct impingement and the surface diffusion pathways in quantitative detail, and analytically model the transition between different transport regimes. Furthermore, we are able to predict the graphene nanopore size limit that is required to achieve meaningful gas separation performances.

Results and Discussion

Theoretical Model

Based on the modeling study by Drahushuk and Strano,[25] we describe the gas permeation process using a three-state reaction kinetics model (Fig. 1). The three states which a gas molecule can occupy include (1) the bulk gas state, characterized by the bulk pressure p, (2) the surface adsorption state, characterized by the areal number density of adsorbed gas molecules C_{surf}, and (3) the pore mouth state, characterized by the number of gas molecules at the pore mouth N_{pore}. The height of the adsorption layer is a parameter in our model which, as discussed in the next subsection, can be determined using MD simulations. The pore mouth state is defined as the cylinder depicted in red in Fig. 1, which has the pore area as its base and the same height as the adsorption layer.

The transport rates to, or from, the three states can be modeled as first order reactions (Fig. 1(b)). The first order assumption is based on the linear dependence of the rate of diffusion on the concentration gradient (Fick's first law). Because the bulk state and the adsorption state have a large area of contact, the molecular exchange between the two states is rapid. Therefore, the bulk pressure p and the adsorbed areal density C_{surf} can be assumed to be in equilibrium:

$$C_{\text{surf}} = H_{\text{surf}} \cdot p \qquad (1)$$

where H_{surf} is the equilibrium constant and is referred to hereafter as the surface Henry's coefficient, because the equilibrium between the bulk gas and the adsorbed phase resembles Henry's law.[32] The surface Henry's coefficient H_{surf} is constant if the linear adsorption isotherm in Eq. (1) holds. In the case of other adsorption isotherms, such as, the Langmuir isotherm or the Brunauer–Emmett–Teller isotherm,[33] H_{surf} depends on the bulk pressure. In this study, the bulk pressure is lower than 15 bar, and therefore, the surface adsorption occupancy is low.[19] As a result, the adsorption isotherms of the gases studied here are in the linear regime (Supporting Information, Figure S1).

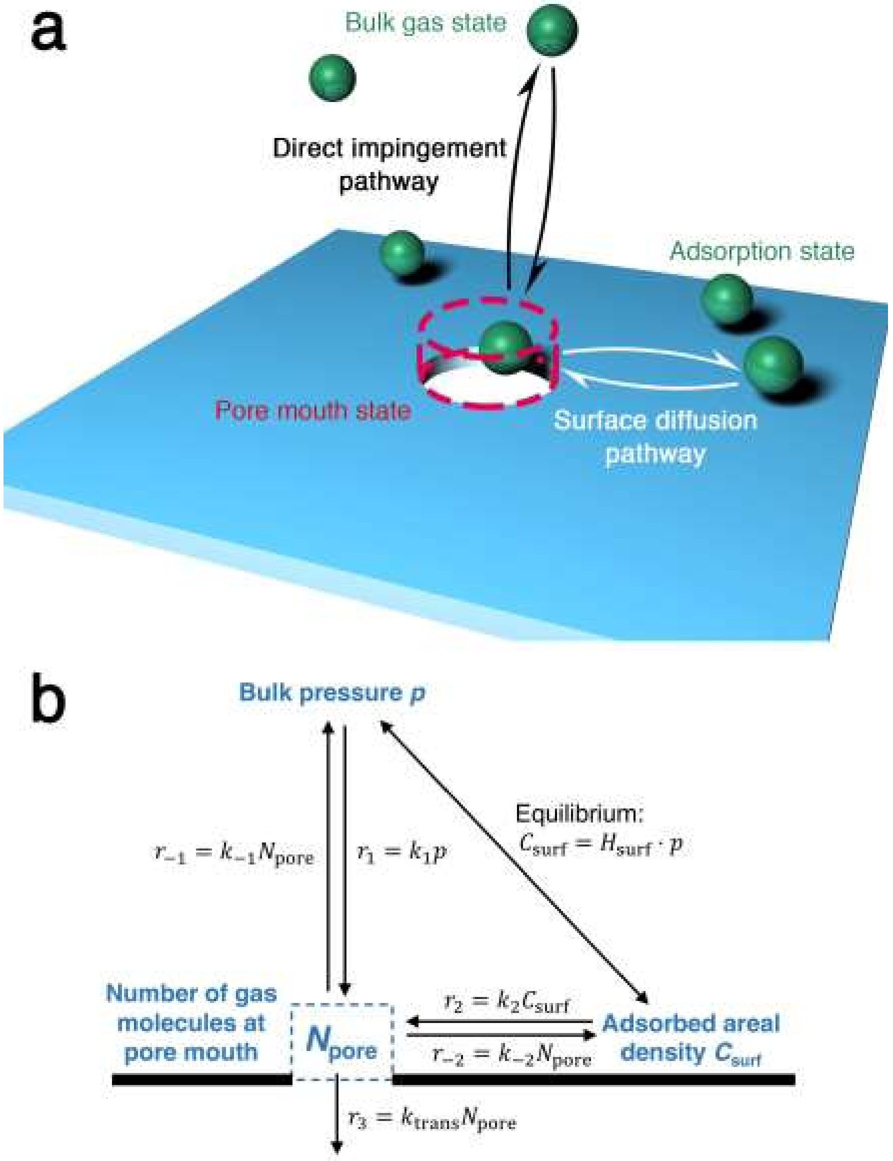

Figure 1: (a) Schematic illustration of the three-state gas permeation model, and (b) its transport rates. The symbols utilized are explained in the main text.

The total gas permeation rate, or the rate of translocation, r_3 is the product of N_{pore} and the translocation coefficient k_{trans} (Fig. 1(b), $r_3 = k_{\mathrm{trans}}N_{\mathrm{pore}}$).[19] The translocation coefficient k_{trans} can be predicted using an algorithm based on the transition state theory developed recently by our group.[19]

We predict that k_{trans} is proportional to exp($-E_a/k_BT$), where E_a is the energy barrier of translocation through the nanopore, k_B is the Boltzmann constant, and T is the absolute temperature. Note that in the current model, we have assumed that the permeate side is vacuum, so that only the feed side pressure needs to be considered. Note also that if the permeate side has a finite pressure, the back-permeance from the permeate side to the feed side can also be treated using the same model.

To fully determine the gas permeation rate r_3, the rate constants k_1, k_{-1}, k_2, and k_{-2} in Fig. 1 need to be specified. The forward rate constant k_1 from the bulk to the pore mouth can be predicted using the kinetic theory of gases. According to the kinetic theory of gases, the impingement rate, r_1, of an ideal gas onto the pore area is expressed as follows:[32]

$$r_1 = A_{\text{pore}}\rho\sqrt{\frac{k_BT}{2\pi m}} \qquad (2)$$

where A_{pore} is the pore area, m is the gas molecular mass, and ρ is the volumetric number density of the bulk gas. In the ideal gas limit, $p = \rho k_BT$. Otherwise, to model a non-ideal gas, the compressibility factor Z needs to be included: $p = Z\rho k_BT$.[32] Continuing with a non-ideal gas and considering a circular pore with diameter D_p, the forward rate constant k_1 can be derived based on Eq. (2), $p = Z\rho k_BT$, and $A_{\text{pore}} = \pi D_p^2/4$:

$$k_1 = \frac{r_1}{p} = \frac{A_{\text{pore}}\rho}{Z\rho k_BT}\sqrt{\frac{k_BT}{2\pi m}} = \frac{A_{\text{pore}}}{Z\sqrt{2\pi m k_BT}} = \sqrt{\frac{\pi}{2mk_BT}}\frac{D_p^2}{4Z} \qquad (3)$$

The expression for the backward rate from the pore mouth to the bulk can be derived as follows. For an elementary reaction, the equilibrium constant is equal to the forward rate constant divided by the reverse rate constant.[34] Therefore, $N_{\text{pore}}^{\text{eqm}}/p = k_1/k_{-1}$, where $N_{\text{pore}}^{\text{eqm}}$ is the number of gas molecules at the pore mouth under the equilibrium condition. We define a pore Henry's coefficient $H_{\text{pore}} = N_{\text{pore}}^{\text{eqm}}/p$ as the equilibrium constant. Following this, the backward rate constant k_{-1} can be derived based on Eq. (3):

$$k_{-1} = k_1\frac{p}{N_{\text{pore}}^{\text{eqm}}} = \frac{k_1}{H_{\text{pore}}} = \sqrt{\frac{\pi}{2mk_BT}}\frac{D_p^2}{4H_{\text{pore}}Z} \qquad (4)$$

Regarding the surface diffusion pathway, Drahushuk and Strano proposed an estimation where the rate of injection from the adsorption layer to the pore r_2 has a similar expression as that in Eq. (2), except that it is proportional to the circumference of the pore, instead of to the pore area, that is:[25]

$$r_2 \propto D_p \qquad (5)$$

In fact, the logic behind the kinetic theory of gases in three-dimensions (3D) can be applied to a two-dimensional (2D) gas system, if we simplify the adsorbed gas molecules as a two-dimensional gas. This simplification is based on the following assumptions: (1) the adsorbed gas molecules have relatively long residence times on the graphene sheet, (2) the adsorbed gas molecules follow the Maxwell-Boltzmann velocity distribution, and (3) the adsorbed gas molecules are evenly distributed on the graphene sheet, excluding the pore mouth area, where the concentration of the gas molecules is lower, leading to surface diffusion of the gas molecules towards the pore mouth area.

Assumption (1) is supported by the simulation study of Sun and Bai,[35] who found that the in-plane diffusion coefficient of the adsorbed gas molecules is lower than that of the gas molecules in the bulk, due to the gas molecule-graphene interactions. Assumption (2) can be directly confirmed by the Maxwell-Boltzmann velocity distribution of the adsorbed gas molecules observed in the MD simulations (Figure S2). Assumption (3) will, in fact, be violated due to the existence of the pore, which complicates the problem. For the sake of simplicity, as a first approximation, we assume that the gases adsorbed on the graphene layer are evenly distributed. However, a more detailed analysis of this underlying assumption will be presented in the next section. Assuming a 2D-gas model for the adsorbed layer, we can neglect the movement of gas molecules in the direction normal to the graphene plane (denoted hereafter as the z direction), and only need to consider the movement of gas molecules parallel to the graphene sheet (denoted hereafter as the x-y plane).

As shown in Fig. 2(a), we consider a differential length dL along the circumference of the pore in the x-y plane. We define the direction tangential to dL as x, and the direction normal to dL as y. According to the Maxwell-Boltzmann distribution, in an orthogonal coordinate system, the velocities of each gas molecule in the x and y directions, v_x and v_y, follow a Gaussian distribution and are independent of each other,[32] that is,

$$f_{v_i}(v_i) = \sqrt{\frac{m}{2\pi k_B T}} \exp\left(-\frac{m v_i^2}{2k_B T}\right) \qquad (6)$$

where $f_{vi}(v_i)$ is the probability density function of v_i, and i corresponds to either the x or the y directions. Using MD simulations, we find that the correlation coefficient of v_x and v_y in the adsorption layer is 0.003, indicating independent velocity distributions in the x and y directions (SI Section 2).

Note that because the velocities v_x and v_y are independent, only v_y matters when considering gas molecules crossing dL in the +y direction (see Fig. 2(a)). For a gas molecule with $v_y > 0$, it can cross dL within a differential time interval dt if the y-projection of its distance to dL is less than v_ydt. In other words, only the molecules in the area $v_y \mathrm{d}t\mathrm{d}L$ are available to be transported across dL. Given the areal density of gas molecules, C_{surf}, the differential number of gas molecules $\mathrm{d}^2 n_2$ crossing $\mathrm{d}L$ in the $+y$ direction during the time interval $\mathrm{d}t$ can be integrated from $v_y = 0$ to $+\infty$:

$$\mathrm{d}^2 n_2 = \int_0^{+\infty} [(v_y \mathrm{d}t) C_{\text{surf}} \mathrm{d}L f_{v_y}(v_y)] \mathrm{d}v_y = \sqrt{\frac{k_B T}{2\pi m}} C_{\text{surf}} \mathrm{d}t \mathrm{d}L \qquad (7)$$

Note that we have used the second differential $\mathrm{d}^2 n_2$ because we need to match the orders of the differential on both sides of Eq. (7). According to Eq. (7), the rate of surface inward diffusion $\mathrm{d}r_2$ across the differential length $\mathrm{d}L$ can be expressed as follows ($r_2 = \mathrm{d}n_2/\mathrm{d}t$):

$$\mathrm{d}r_2 = \mathrm{d}\left(\frac{\mathrm{d}n_2}{\mathrm{d}t}\right) = \sqrt{\frac{k_B T}{2\pi m}} C_{\text{surf}} \mathrm{d}L \qquad (8)$$

Note that Eq. (8) is valid for any differential length $\mathrm{d}L$ along the pore rim. Therefore, by integrating $\mathrm{d}r_2$ over the circumference of the pore $L = \pi D_p$, we obtain:

$$r_2 = \oint_L \mathrm{d}r_2 = \oint_L \sqrt{\frac{k_B T}{2\pi m}} C_{\text{surf}} \mathrm{d}L = \sqrt{\frac{k_B T}{2\pi m}} C_{\text{surf}} L = \sqrt{\frac{\pi k_B T}{2m}} C_{\text{surf}} D_p \qquad (9)$$

Note that Eq. (9) is consistent with Eq. (5). The forward rate constant associated with the surface diffusion pathway k_2 is therefore given by:

$$k_2 = \frac{r_2}{C_{\text{surf}}} = \sqrt{\frac{\pi k_B T}{2m}} D_p \qquad (10)$$

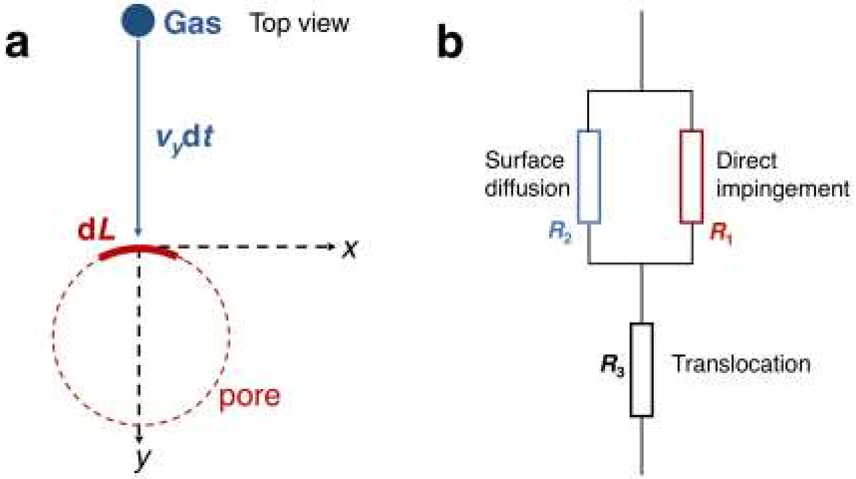

Figure 2: (a) Derivation of the rate of injection from the adsorption layer to the pore. Injection is an essential step in the surface diffusion pathway. (b) Transport resistances associated with the translocation, the surface diffusion, and the direct impingement steps are represented in an analogous electric circuit form.

The backward rate constant k_{-2} from the pore to the adsorption layer can be derived in a manner similar to that used to derive k_{-1} in the direct impingement pathway. The equilibrium constant between the surface adsorption state (areal adsorption density C_{surf}) and the pore mouth state (pore mouth molecular number N_{pore}) is equal to the forward rate constant k_2 divided by the reverse rate constant k_{-2}.[34] Therefore, $N_{\mathrm{pore}}^{\mathrm{eqm}}/C_{\mathrm{surf}} = k_2/k_{-2}$, where $N_{\mathrm{pore}}^{\mathrm{eqm}}$ is the number of gas molecules at the pore mouth under the equilibrium condition. Recall that we previously defined the surface Henry's coefficient $H_{\mathrm{surf}} = C_{\mathrm{surf}}/p$ (Eq. (1)) and the pore Henry's coefficient $H_{\mathrm{pore}} = N_{\mathrm{pore}}^{\mathrm{eqm}}/p$. Therefore, we can derive the backward rate constant k_{-2} as follows:

$$k_{-2} = k_2 \frac{C_{\mathrm{surf}}}{N_{\mathrm{pore}}^{\mathrm{eqm}}} = k_2 \frac{C_{\mathrm{surf}}/p}{N_{\mathrm{pore}}^{\mathrm{eqm}}/p} = k_2 \frac{H_{\mathrm{surf}}}{H_{\mathrm{pore}}} = \sqrt{\frac{\pi k_B T}{2m}} \frac{H_{\mathrm{surf}}}{H_{\mathrm{pore}}} D_p \qquad (11)$$

Knowing the rate constants k_1, k_{-1}, k_2, and k_{-2}, we can derive the overall gas permeation rate as follows. At steady state, the number of gas molecules at the pore mouth should be time invariant:

$$\frac{\mathrm{d}N_{\mathrm{pore}}}{\mathrm{d}t} = r_1 - r_{-1} + r_2 - r_{-2} - r_3 = 0 \qquad (12)$$

where

$$r_1 = k_1 p = \sqrt{\frac{\pi}{2mk_BT}} \frac{D_p^2}{4Z} p \qquad (12a)$$

$$r_{-1} = k_{-1} N_{\mathrm{pore}} = \sqrt{\frac{\pi}{2mk_BT}} \frac{D_p^2}{4H_{\mathrm{pore}}Z} N_{\mathrm{pore}} \qquad (12b)$$

$$r_2 = k_2 C_{\mathrm{surf}} = k_2 H_{\mathrm{surf}} p = \sqrt{\frac{\pi k_B T}{2m}} D_p H_{\mathrm{surf}} p \qquad (12c)$$

$$r_{-2} = k_{-2} N_{\mathrm{pore}} = \sqrt{\frac{\pi k_B T}{2m}} \frac{H_{\mathrm{surf}}}{H_{\mathrm{pore}}} D_p N_{\mathrm{pore}} \qquad (12d)$$

$$r_3 = k_{\mathrm{trans}} N_{\mathrm{pore}} \qquad (12e)$$

Using Eqs. (12a) – (12e) in Eq. (12), we obtain:

$$k_1 p - k_{-1} N_{\mathrm{pore}} + k_2 H_{\mathrm{surf}} p - k_{-2} N_{\mathrm{pore}} - k_{\mathrm{trans}} N_{\mathrm{pore}} = 0 \qquad (12f)$$

$$N_{\mathrm{pore}} = p \frac{k_1 + k_2 H_{\mathrm{surf}}}{k_{-1} + k_{-2} + k_{\mathrm{trans}}} \qquad (12g)$$

Using the relations $k_{-1} = \frac{k_1}{H_{\mathrm{pore}}}$ (Eq. (4)) and $k_{-2} = k_2 \frac{H_{\mathrm{surf}}}{H_{\mathrm{pore}}}$ (Eq. (11)), we can rewrite Eq. (12g) as follows:

$$N_{\mathrm{pore}} = p \frac{k_1 + k_2 H_{\mathrm{surf}}}{\frac{k_1 + k_2 H_{\mathrm{surf}}}{H_{\mathrm{pore}}} + k_{\mathrm{trans}}} = p \frac{1}{\frac{1}{H_{\mathrm{pore}}} + \frac{k_{\mathrm{trans}}}{k_1 + k_2 H_{\mathrm{surf}}}} = \frac{1}{\frac{1}{k_1 + k_2 H_{\mathrm{surf}}} + \frac{1}{k_{\mathrm{trans}} H_{\mathrm{pore}}}} \cdot \frac{p}{k_{\mathrm{trans}}} \qquad (13)$$

We define the overall transport resistance R as the ratio between the pressure p and the overall transport rate r_3. Note that R can be interpreted as the inverse of the pressure-normalized flow rate. Using the expression for N_{pore} given in Eq. (13), we obtain:

$$R = \frac{p}{r_3} = \frac{p}{k_{\text{trans}} N_{\text{pore}}} = \frac{1}{k_1 + k_2 H_{\text{surf}}} + \frac{1}{k_{\text{trans}} H_{\text{pore}}} \qquad (14)$$

Note that each term in the denominators of the fractions in Eq. (14) can be regarded as a transport resistance, corresponding to each transport step, that is,

$$R_1^{-1} = k_1 = \sqrt{\frac{\pi}{2mk_BT}}\frac{D_p^2}{4Z} \qquad (15)$$

$$R_2^{-1} = k_2 H_{\text{surf}} = \sqrt{\frac{\pi k_B T}{2m}} D_p H_{\text{surf}} \qquad (16)$$

$$R_3^{-1} = k_{\text{trans}} H_{\text{pore}} \qquad (17)$$

Based on Eqs. (15)-(17), Eq. (14) can be conveniently rewritten as follows:

$$R = R_3 + \frac{1}{\frac{1}{R_1} + \frac{1}{R_2}} \qquad (18)$$

Note that R_1, R_2, and R_3 represent the innate kinetics associated with each transport step. Indeed, R_1 is the resistance associated with the direct impingement step, R_2 is the resistance associated with the surface diffusion step, and R_3 is the resistance associated with the translocation step. Therefore, the overall resistance associated with these three steps is modeled by R_1 and R_2 being in parallel, and their combination being in series with R_3 (see Figure 2(b)).

Equations (14)-(18) provide important insights into the dependence of the gas flow rate on the pore diameter D_p. When D_p is approximately equal to the gas kinetic diameter D_m, the translocation energy barrier E_a leads to an extremely small translocation coefficient k_{trans}, where $k_{\text{trans}} \propto \exp\left(-\frac{\mathrm{E_a}}{k_BT}\right)$ and a large R_3. Wang *et al.* proposed that the energy barrier $E_a \approx \sqrt{\frac{4\pi\varepsilon D_p}{a}}\left(\frac{2\sigma}{D_p}\right)^{12}$, where ε and σ are Lennard-Jones parameters that approximate the gas molecule-pore interaction, and a is the distance between adjacent atoms on the pore rim.[26] The distance parameter σ in the Lennard-Jones potential is strongly correlated to the gas kinetic diameter D_m, and therefore, the energy barrier increases significantly as D_m approaches, or even exceeds, D_p. For better accuracy, k_{trans} and R_3 should be treated as implicit functions of D_m and D_p, and these values can be obtained using all-atomistic MD simulations.[19]. In cases where R_3 is large, the translocation resistance R_3 is dominant ($R \approx R_3$) because it is much greater than both R_1 and R_2, and our model can reproduce the activated regime in the small pore limit. In the activated regime, the size of the pore becomes discretized, and pore features like shape and eccentricity can strongly affect its barrier properties.

On the other hand, when D_p is sufficiently large relative to D_m (but still smaller than the gas mean free path), the pore edge no longer imposes a translocation energy barrier and R_3 is small and negligible. As $D_m/D_p \rightarrow 0$, $\sigma/D_p \rightarrow 0$, and the energy barrier $E_a \rightarrow 0$. Considering the direct impingement (R_1^{-1}) and surface diffusion (R_2^{-1}) pathways, R_1^{-1} scales as D_p^2 (see Eq. (15)) and R_2^{-1} scales as D_p (see Eq. (16)). Therefore, in the large pore limit, $R_1^{-1} \gg R_2^{-1}$, and the direct impingement pathway is dominant ($R \approx R_1$), which reproduces the effusion mechanism. It is noteworthy that R_1, R_2, and R_3 exhibit different temperature dependences. To further study the role of temperature on gas permeation, we have carried out MD simulations at different temperatures to probe the physical nature of the transport steps (see the next subsection).

The theoretical permeation model introduced above was based on several assumptions, including 100% permeation success probability, and is expected to demonstrate deviations from real practical situations. More specifically, the permeation model requires revision, validation, and calibration due to the following reasons. First, the rate of surface diffusion depends on the value of the surface Henry's coefficient H_{surf}. It is still an open question whether the surface diffusion step is rate determining, and if it is, under what conditions. Second, the equations proposed above may require some corrections associated with potential nonidealities of the gases considered which need to be accounted for. For example, the diffusion of a gas molecule from the adsorption layer to the pore mouth could also require overcoming an energy barrier.[19,25] This energy barrier along the surface diffusion path, in turn, would reduce the flow rate of gas from the adsorption layer to the pore mouth. Third, there may be additional pathways, or mechanisms, that were not considered in our model. For example, the direct impingement and the surface diffusion pathways can potentially interfere with each other. In the next subsection, we will utilize MD simulations to test the validity of our gas permeation model, including refining it as needed.

Molecular Dynamics Simulation Results

In order to test the validity of our transport model, we carried out MD simulations to estimate the gas permeation rate and to study its dependence on the pore size (see Methods section for more details). As shown in Fig. 3(a), a typical simulation run was carried out in a 10 × 10 × 80 nm^3 simulation box, separated into two identical compartments by two 10 × 10 nm^2 graphene sheets placed parallel to each other, with one hydrogen-terminated pore on each sheet. The two compartments had the same number of gas molecules and were in equilibrium at the beginning of the simulation (see Fig. 3(a)). The number of permeation events in both directions was counted by analyzing the trajectories of all the gas molecules. Due to the rarity of gas-gas collisions in the dilute gas limit, the one-sided non-equilibrium permeation rate is one half of the two-sided equilibrium permeation rate. This strategy was introduced and justified by Sun *et al*.[30] Because the simulation box contains two porous graphene sheets, the one-sided gas flow rate through one membrane was one quarter of the two-sided flow rate in the entire simulation box.

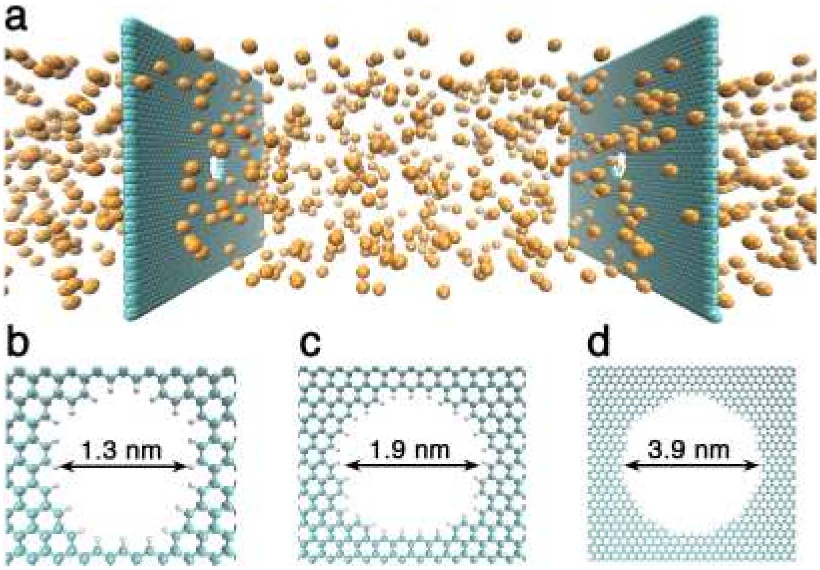

Figure 3: (a) Snapshot of the MD simulation measuring Ar permeation through graphene pores of 1.3 nm diameter. (b-d) Atomic structures of the 1.3 nm, 1.9 nm, and 3.9 nm diameter graphene nanopores, respectively. Color code: cyan–C, white–H, orange–Ar.

We simulated gas permeation through three types of nanopores, with diameters of 1.3, 1.9, and 3.9 nm, respectively (Fig. 3(b)-(d)). These pores are sufficiently large relative to the kinetic diameters of the three gases considered (CO_2: 0.33 nm, Ar: 0.34 nm, and CH_4: 0.38 nm).[20] As a result, there is no translocation energy barrier, resulting in a low translocation resistance ($R_3 \approx 0$). Therefore, Eq. (18) can be rewritten as follows:

$$R^{-1} = R_1^{-1} + R_2^{-1} = k_1 + k_2 H_{\mathrm{surf}} = \sqrt{\frac{\pi}{2mk_BT}}\frac{D_p^2}{4Z} + \sqrt{\frac{\pi k_BT}{2m}} D_p H_{\mathrm{surf}} \qquad (19)$$

where Eqs. (15) and (16) were used. Note that R^{-1} is also defined as the pressure-normalized permeation rate, with a unit of mol s^{-1} Pa^{-1} (or molecule s^{-1} Pa^{-1}). Because in the discussions which follow, we will refer to the transport resistances R, R_1, and R_2 mainly in the inverse form, for simplicity, we introduce the total permeance per pore $K = R^{-1} = r_3/p$. It is worth noting that the definition of "permeance per pore" adopted here is different from the common definition of permeance as the pressure-normalized gas flux (with a unit of mol s^{-1} Pa^{-1} m^{-2}). Note also that the conventional permeance, as well as the permeance per pore, are simply related through the areal pore density. Following our definition, we define the permeance per pore associated with the direct impingement pathway as K_1, and that associated with the surface diffusion pathway as K_2. According to our model, we partition the total permeance per pore into its two contributions, K_1 and K_2, as follows (derived from Eq. (19)):

$$K = R^{-1} = R_1^{-1} + R_2^{-1} = k_1 + k_2 H_{\text{surf}} = K_1 + K_2 \tag{20}$$

$$K_1 = k_1 = \sqrt{\frac{\pi}{2mk_BT}}\frac{D_p^2}{4Z} \tag{21}$$

$$K_2 = k_2 H_{\text{surf}} = \sqrt{\frac{\pi k_BT}{2m}} D_p H_{\text{surf}} \tag{22}$$

In order to compare our simulation results with Eqs. (20)-(22), the permeation events observed in the MD simulations need to be partitioned into those associated with the direct impingement pathway (referred to as the “direct pathway” in the figures) and with the surface diffusion pathway (referred to as the “surface pathway” in the figures). To this end, we consider a permeation event to be associated with the direct impingement pathway if the gas molecule moves into the pore mouth cylinder state from the top and then crosses the pore (Fig. 1). Otherwise, if the gas molecule moves into the pore mouth cylinder state from the side and then crosses the pore, the permeation event is associated with the surface diffusion pathway. The height of the cylinder pore mouth state was set at 0.7 nm, which is consistent with the thickness of the surface adsorption layer (Fig. S3). Although the choice of this height can affect the partition of the permeation events, the effect is minor (Fig. S4). The pressure and the compressibility factor resulting from each simulation were calculated by the equations of state provided by the open source program CoolProp.[36] In our simulations, the most non-ideal compressibility factor Z is 0.96, obtained for CO_2 at $T = 300$ K and $p = 7.2$ bar, which is close to the ideal gas limit ($Z = 1$). This finding indicates that all our MD simulations were carried out near the ideal gas condition.

Figure 4 shows how the gas permeation depends on pressure, temperature, and pore diameter, as well as on the contributions from the direct impingement and the surface diffusion pathways, all obtained from the MD simulations. As shown in Fig. 4(a), the total permeances per pore of the three gases considered are independent of pressure up to ∼10 bar. This suggests that the parameters in Eqs. (20)-(22) are independent of pressure. The error bars (95% confidence intervals) were obtained by assuming that each permeation event occurs independently and randomly, and that the total number of permeation events follows a Poisson distribution. The equation used to calculate the confidence interval (SI Section S4) indicates that a greater number of total permeation events leads to a lower error. Accordingly, in the remainder of our study, unless stated specifically, because the total number of permeation events is proportional to the pressure, we chose the highest pressure for each gas in order to minimize the relative errors (see Fig. 4(a)). Figure 4(b) shows that the gas permeance per pore decreases as the temperature increases. This is due to the fact that the contributions from the direct impingement and the surface diffusion pathways are both decreasing functions of temperature (see below). Note that the gas permeance per pore increases non-linearly with the pore diameter (Fig. 4(c)), and that the contributions from the direct impingement and the surface diffusion pathways increase differently with increasing pore diameter (Fig. 4(d)). Specifically, the direct impingement pathway permeance per pore scales non-linearly with pore diameter (as predicted by Eq. (21)), while the surface diffusion pathway permeance per pore scales nearly linearly with pore diameter (as predicted by Eq. (22), and shown by the blue dashed line, Fig. 4(d)). The cases corresponding to CH_4 and Ar are similar, and are shown in Fig. S5.

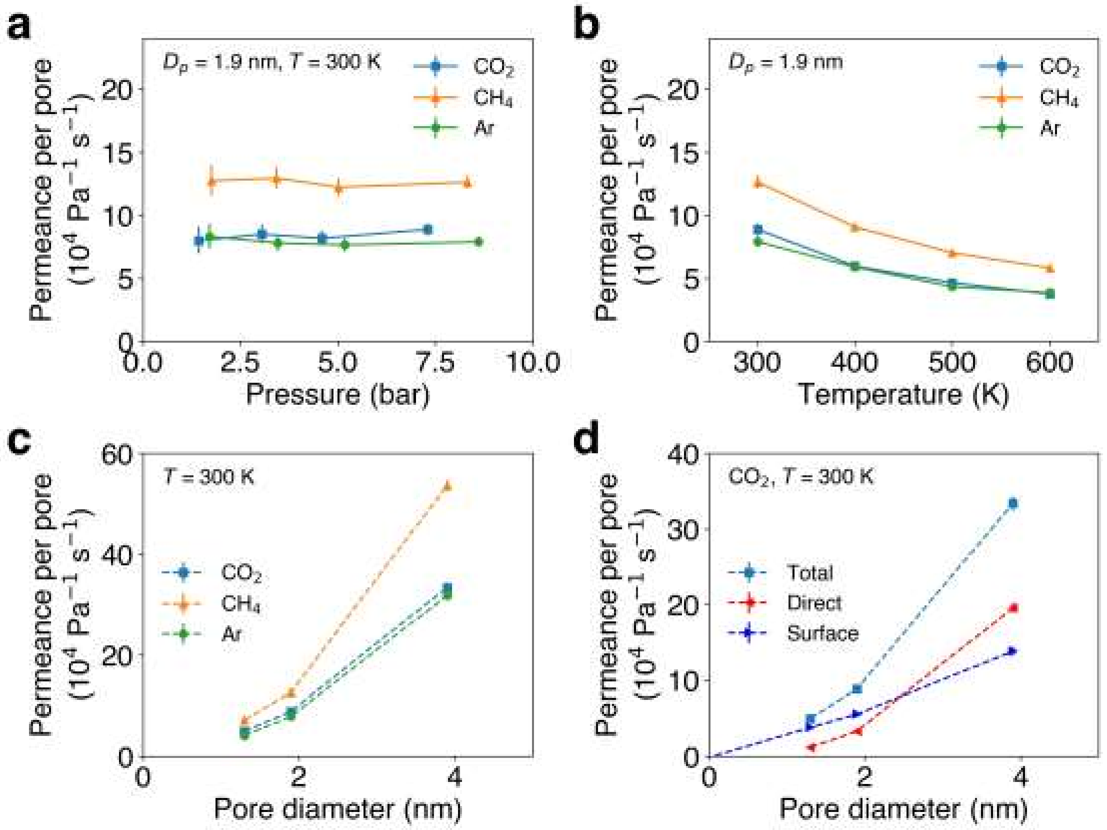

Figure 4: Total permeances per pore of CO_2, CH_4, and Ar through 1.9-nm pore at (a) various pressures and (b) various temperatures. (c) Permeances per pore of CO_2, CH_4, and Ar as functions of the pore diameter at 300 K. (d) Contributions of the direct impingement and the surface diffusion

pathways to the total CO_2 permeance per pore as a function of the pore diameter at 300 K.

Figure 5 provides additional details about the direct impingement pathway. The permeance per pore contributed by the direct impingement pathway mildly decreases with increasing temperature (Fig. 5(a)), which is consistent with our theoretical prediction (Eq. (21)). Furthermore, Eq. (21) (green dashed line, Fig. 5(b)) can predict the rate of direct impingement attempts of CO_2 with a slight underestimation relative to the MD simulation result (orange dashed line, Fig. 5(b)). However, the theory (green dashed line, Fig. 5(b)) overpredicts the actual permeance per pore (blue dashed line, Fig. 5(b)), because only a fraction of the direct impingement attempts results in successful permeation. In fact, the majority of the direct impingement attempts to the pore mouth area do not lead to permeation. The situation is similar for CH_4 and Ar (Fig. S6 (a), (b)).

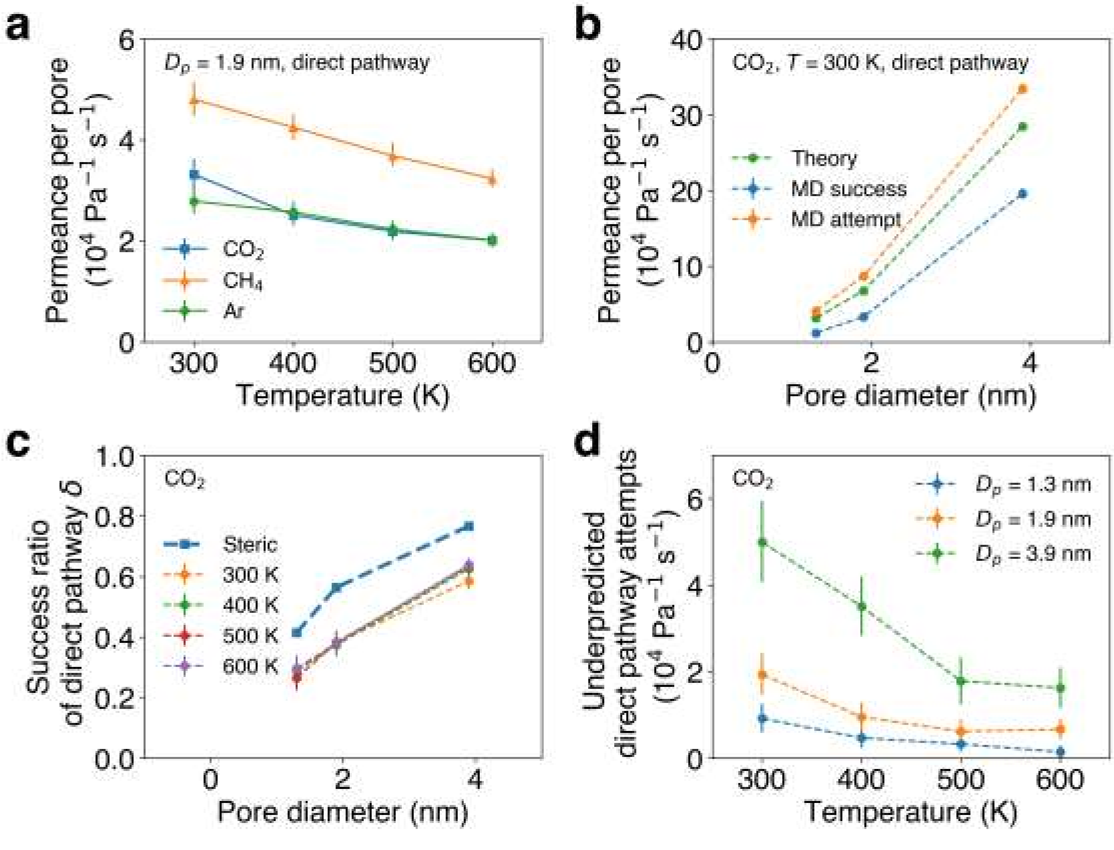

Figure 5: (a) Permeance per pore contributed by the direct impingement pathway as a function of temperature for CO_2, CH_4, and Ar. (b) Comparison of the permeance per pore contributed by the direct impingement pathway obtained using MD simulations and our theory for CO_2 at 300 K. (c) Comparison of the success ratio of the direct impingement pathway obtained using MD simulations and the steric selectivity theory proposed in our previous work[7] for CO_2 as a function of pore

diameter at various temperatures. (d) Deviation of our theoretical predictions (Eq. (21)) from the MD simulation-observed permeation attempts for CO_2 as a function of temperature for various pore diameters.

The discrepancy between the permeation rate and the attempt rate observed in MD simulations indicates that a factor δ which is smaller than unity needs to be introduced to correct the theoretical prediction associated with the direct impingement rate. Indeed, a fraction of these attempts fail because a gas molecule can collide with the pore edge and bounce off.[26] Therefore, δ is defined as the ratio between the successful permeation rate and the attempt rate associated with the direct impingement pathway obtained in the MD simulations. For a given gas, this effect is expected to be less pronounced as the pore diameter increases. The success ratio δ of CO_2 increases from 0.3 to 0.6 as the pore diameter increases from 1.3 to 3.9 nm (Fig. 5(c)). As the pore diameter increases further, for a given gas, δ should approach unity. This correlation is independent of temperature (see the four curves corresponding to 300, 400, 500, and 600 K for CO_2 in Fig. 5(c)). A similar trend holds in the case of CH_4 and Ar (Fig. S6(c), (d)). In fact, we explored this phenomenon in detail in our recent combined experimental and theoretical study, and referred to it as the steric selectivity mechanism.[7] We also showed that the success ratio δ can be approximated as follows:[7]

$$\delta = \left(1 - \frac{D_m}{D_p}\right)^3 \qquad (23)$$

The prediction made using Eq. (23), denoted as "steric" in Fig. 5(c), considers the distribution of the angle of incidence. Alternatively, if all the impingement attempts are assumed to be normal to the graphene plane, the success ratio can be approximated as $\delta = (1 - D_m/D_p)^2$. However, Figure 5(c) shows that Eq. (23) (the blue dashed line) overestimates the success ratio δ relative to the MD simulation results (the other four almost overlapping lines), suggesting that additional factors reduce the success ratio. For example, the trajectory of an impingement attempt may be distorted towards the pore edge due to the van der Waals interactions exerted by the pore edge atoms, which would decrease the likelihood of a successful crossing. Note that in the steric selectivity mechanism,[7] the impingement trajectories of the gas molecules are assumed to be straight and unaffected by the van der Waals attractive forces. Because of the expected molecular-level complexity of the gas-pore interaction, we propose a semi-empirical equation for the success ratio, inspired by Eq. (23):

$$\delta = \left(1 - \frac{D_m}{D_p}\right)^\alpha \qquad (24)$$

Interestingly, the proposed equation can reproduce the limiting cases: (i) $D_m = 0$ leads to $\delta = 1$ (no reduction in the success ratio due to gas molecule-pore collision), and (ii) $D_m = D_p$ leads to $\delta = 0$ (zero success ratio due to 100% likelihood of collision). We fit $\ln(\delta)$ *vs.* $(1 - D_m/D_p)$ using a linear correlation, and the fitting results show that the exponent α in Eq. (24) is different for the three gases considered: $\alpha(CO_2) = 4.58$ ($R^2 = 0.93$), $\alpha(CH_4) = 3.68$ ($R^2 = 0.95$), and $\alpha(Ar) = 4.32$ ($R^2 = 0.97$). We found no obvious correlation between the value of α and the properties of the three gases considered, including their kinetic diameters and Lennard-Jones parameters. Nevertheless, all the three α values are greater than 3 in the steric selectivity mechanism,[7] indicating an enhanced gas molecule-pore edge interaction relative to that predicted by our original model.

It is also noteworthy that Eq. (21) underestimates the rate of direct impingement attempts relative to the MD simulation results. Indeed, in Fig. 5(d), we plot the difference between the simulated and the predicted direct pathway impingement attempts as a function of temperature for CO_2 and three pore diameters. Interestingly, Fig. 5(d) shows that the difference is a decreasing function of temperature and an increasing function of the pore diameter, instead of being random. This trend is also observed for CH_4 and Ar (Fig. S6(e), (f)). This difference (Fig. 5(d)) is one order of magnitude lower than the rate of the simulated direct impingement attempts (Fig. 5(b)). This finding suggests that the difference between the simulated and the theoretical results reflects the existence of a separate minor permeation pathway. We will discuss this fourth transport pathway below, but first, we will further examine the surface diffusion pathway.

The gas permeance contributed by the surface diffusion pathway decays rapidly with increasing temperature for $D_p = 1.9$ nm (see Fig. 6(a)). This is mainly due to the exothermic gas molecule-graphene adsorption contributed by the van der Waals interaction. Similar observations can be made for $D_p = 1.3$ nm and $D_p = 3.9$ nm (Fig. S7(a), (b)). The surface Henry's coefficient H_{surf} represents the magnitude of the gas adsorption on the graphene surface, and it is correlated to temperature according to the van't Hoff equation, involving the heat of adsorption ΔH_{ads}.[32] Specifically,

$$H_{\text{surf}}(T) = H_{\text{surf}}^{0} \exp\left(-\frac{\Delta H_{ads}}{k_B T}\right) \tag{25}$$

where H_{surf}^{0} is the prefactor. Heat of adsorption values for the three gases considered were derived by fitting $H_{\text{surf}}(T)$ obtained from MD simulations to Eq. (25), within the temperature range from 300 to 600 K, and are listed in Table 1.

Table 1: Heats of adsorption and energy barriers of injection for CO_2, CH_4, and Ar within the temperature range T = 300 to 600 K (see the text for details).

	Heat of adsorption ΔH_{ads} (kJ mol^{-1})	Energy barrier associated with injection $E_{a,\mathrm{inj}}$ (kJ mol^{-1})		
		D_p = 1.3 nm	D_p = 1.9 nm	D_p = 3.9 nm
CO_2	-10.7 ± 0.5	2.2	2.3	2.7
CH_4	-9.2 ± 0.6	1.9	2.0	2.2
Ar	-7.9 ± 1.0	2.2	2.0	2.4

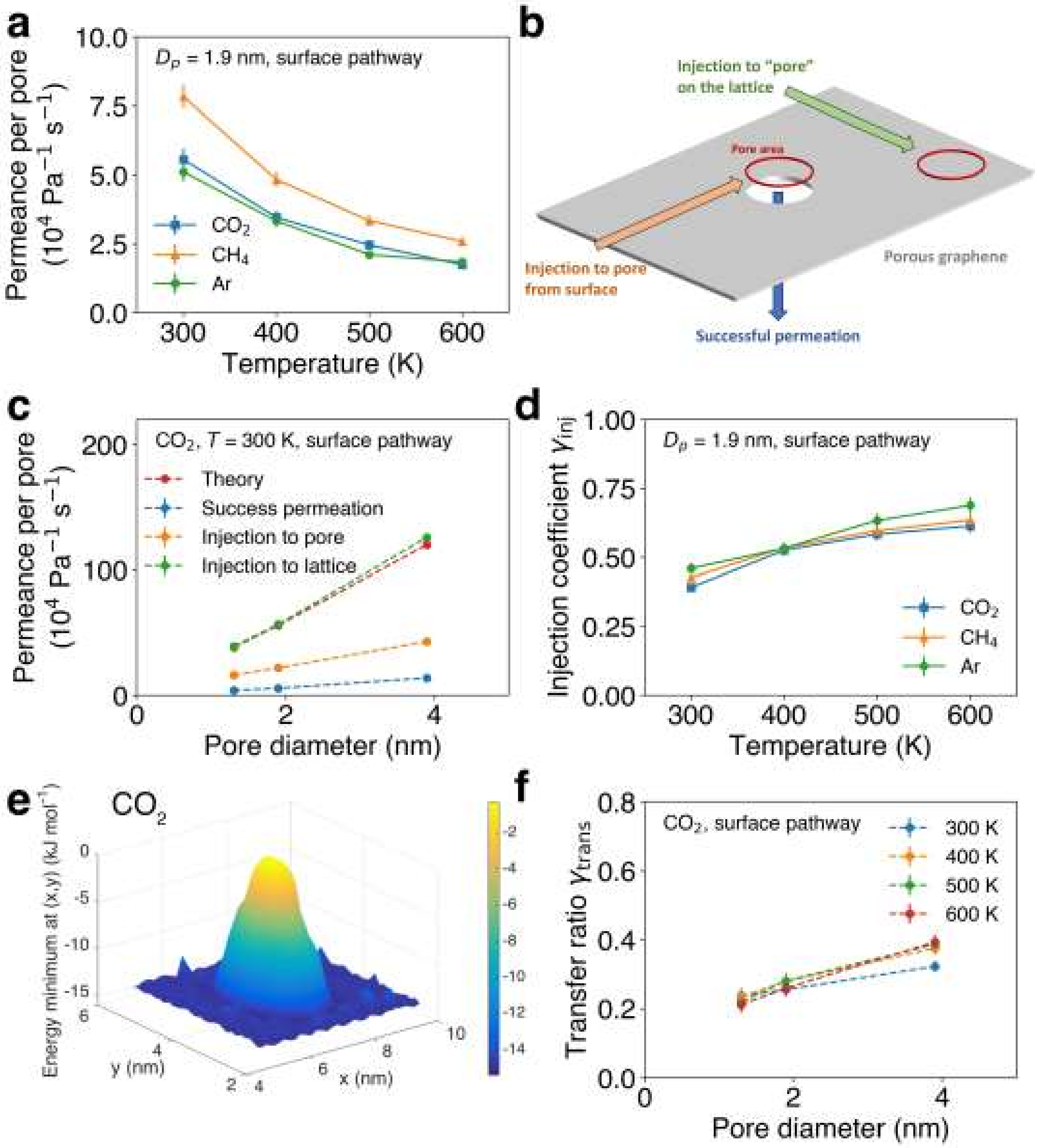

Figure 6: (a) Permeance per pore contributed by the surface diffusion pathway as a function of temperature for CO_2, CH_4, and Ar. (b) Schematic illustration of monitored transport rates

associated with the surface diffusion pathway. (c) Comparison of the permeance per pore contributed by the surface diffusion pathway obtained using MD simulations and our theoretical predictions as a function of pore diameter for CO_2 *at* $T = 300$ *K. (d) Injection coefficient corresponding to the surface diffusion pathway* γ_{inj} *as a function of temperature for the three gases considered for* $D_p = 1.9$ *nm. (e) Potential energy landscape of a* CO_2 *molecule near the 1.9-nm diameter graphene pore. The peak represents a rise in energy above the pore. (f) Transfer ratio corresponding to the surface diffusion pathway* γ_{trans} *as a function of pore diameter for* CO_2 *at various temperatures.*

In order to analyze the surface diffusion pathway, we can further identify two individual steps along this pathway (see the orange and blue arrows in Fig. 6(b)). Firstly, a gas molecule adsorbed on the graphene surface injects into the pore mouth area (orange arrow in Fig. 6(b), denoted as "injection to pore" in Fig. 6(c)). Subsequently, the injected molecule permeates through the pore (blue arrow in Fig. 6(b), denoted as "success permeation" in Fig. 6(c)). It is worth noting that the rates of both steps are significantly lower than the theoretical prediction provided by Eq. (22) (denoted as "theory" in Fig. 6(c)). Interestingly, if we move the "pore area" away from the physical pore in the graphene lattice and monitor the gas injection rate as if the pore were located at a new location (green arrow in Fig. 6(b)), the rate of injection to the "fictitious pore" in the lattice (denoted as "injection to lattice", green dashed curve in Fig. 6(c)) matches the theoretical prediction (denoted as "theory", red dashed curve in Fig. 6(c)). Note that this fictitious pore injection rate is independent of the fictitious pore—real pore distance when it is greater than 5 nm. Therefore, in the first step along the surface diffusion pathway, a fraction of the injection attempts is rejected. In addition, in the second step, among the gas molecules that arrive at the pore mouth area, only a fraction permeates through the pore. This behavior is similar for CH_4 and Ar (Fig. S7(c), (d)). We denote the first success ratio as the injection coefficient γ_{inj}, and the second success ratio as the transfer ratio γ_{trans}.

As shown in Fig. 6(d), the injection coefficient γ_{inj} for $D_p = 1.9$ nm is an increasing function of temperature, indicating that the injection step is associated with climbing an energy barrier (similar results are obtained for the two other pore diameters, see Fig. S7(e), (f)). Figure 6(e) shows the potential energy landscape of CO_2 adsorbing on graphene in the vicinity of the pore. The potential energy increases as the CO_2 molecule moves above the pore region, because the carbon atoms missing from the graphene lattice, due to the presence of the pore, are not able to interact favorably with the gas molecules *via* van der Waals interactions. In other words, an adsorbed gas molecule needs to "desorb" from the graphene lattice to enter the pore area, which involves an energy barrier. In the case of CH_4 and Ar, as well as of the two other pore sizes considered, the potential energy landscapes are similar to that in Fig. 6(e), with varying heights and basal areas of the potential energy protrusion. This energy barrier violates the assumptions underlying Eq. (22) because the gradient in the potential energy landscape felt by the gas molecules disrupts their in-plane distribution. The energy barriers associated with injection $E_{a,\mathrm{inj}}$ for the three gases considered can be derived by fitting the three injection coefficients γ_{inj} to temperature according to an Arrhenius equation. Specifically,

$$\gamma_{\mathrm{inj}} = \gamma_{\mathrm{inj}}^{0} \exp\left(-\frac{E_{a,inj}}{k_B T}\right) \qquad (26)$$

where $\gamma_{\mathrm{inj}}^{0}$ is the prefactor. The energy barriers associated with injection into pores for the three gases considered having values of D_p equal to 1.3, 1.9, and 3.9 nm, respectively, are listed in Table 1. Because of the "desorbing" nature of the injection step, the energy barrier associated with injection should be correlated to the heat of adsorption. Note that for the three pore diameters considered, the energy barrier associated with injection $E_{a,\mathrm{inj}}$ is 20–30% of the heat of adsorption ΔH_{ads} (absolute value). This is because the gas molecule only needs to climb less than halfway on the energy bump to enter the pore region. The fitted values of the prefactor $\gamma_{\mathrm{inj}}^{0}$ in Eq. (26) for the nine cases considered (three gases and three pores) are close to 1 (1.00 ± 0.11). Therefore, we can assume that $\gamma_{\mathrm{inj}}^{0} \approx 1$. If $E_{a,\mathrm{inj}}$ approaches 0, γ_{inj} approaches its maximum value of 1, which is consistent with the definition of γ_{inj} as a success ratio between 0 and 1.

The transfer ratio γ_{trans} characterizes the success ratio associated with a gas molecule crossing the membrane *if* it has entered the pore area. Although some gas molecules may have entered the pore area, they could have slided across the pore without permeating through the pore. As shown in Fig. 6(f), γ_{trans} for CO_2 is quite independent of temperature, and therefore, this second step does not involve climbing an energy barrier. For CH_4 and Ar, similar observations can be made (Fig. S7(g), (h)). In addition, γ_{trans} is positively correlated to the pore diameter (Fig. 6(f), Fig. S7(g), (h)), which is expected because a larger pore is more likely to allow gas permeation. It is noteworthy that a theoretical prediction of γ_{trans} is challenging, because the momentum change which drives a gas molecule to cross the pore involves complex gas–pore and gas–gas collisions. Nevertheless, we can gain additional insight by considering the following two limiting cases – (1) when D_p approaches 0 (D_m/D_p approaches infinity), γ_{trans} should approach 0 because the pore is closed, and (2) when D_p

approaches infinity (D_m/D_p approaches 0), γ_{trans} is expected to approach 0.5 because the gas molecule has equal probability to move towards, or to move away from, the pore in the z direction.

Recall that in the direct impingement pathway analysis, Eq. (21) underpredicts the rate of the direct impingement attempts relative to the simulation results, with the deviation showing a sharp decrease with increasing temperature (Fig. 5(d)). This negative correlation with temperature resembles the temperature dependence of the permeance *via* the surface diffusion pathway (Fig. 6(a)). Therefore, we hypothesize that the surplus direct impingement attempts observed in our MD simulations originate from the adsorption layer. In order to test this hypothesis, we analyzed the angle of incidence distribution among all the permeation events as follows. The angle of incidence is defined as the angle formed between the direction normal to the graphene plane (+z) and the tangent to the molecule's trajectory at the point of crossing the graphene basal plane (z = 0), as shown in the inset at the top-right in Fig. 7(a). We assume that the crossing occurs at time t_0. In that case, the angle of incidence θ can be derived from the velocity $\vec{v}$ of a gas molecule at the crossing point:

$$\theta = \tan^{-1}\left(\frac{|v_z|}{\sqrt{v_x^2+v_y^2}}\right) \qquad (27)$$

Because the trajectories recorded in the MD simulations are discretized in time, we need to use the secant between times t_0 and $t_0-\Delta t$ to replace the tangent at t_0, where Δt is a small time interval. Therefore, the angle of incidence obtained from our simulations should be calculated as follows:

$$\theta = \tan^{-1}\left\{\frac{\frac{z(t_0)-z(t_0-\Delta t)}{\Delta t}}{\sqrt{\left[\frac{x(t_0)-x(t_0-\Delta t)}{\Delta t}\right]^2+\left[\frac{y(t_0)-y(t_0-\Delta t)}{\Delta t}\right]^2}}\right\} \qquad (28)$$

Note that in the limit of $\Delta t \to 0$, Eq. (28) reduces to Eq. (27). Interestingly, Δt can be carefully tuned to reveal additional mechanistic details. For example, we can use the angle of incidence to determine whether a permeated gas molecule originates from the bulk gas phase or from the adsorption layer. To this end, the average distance $\bar{v}\Delta t$ traversed by a gas molecule having average speed $\bar{v}$ during time Δt should satisfy the following requirements. First, $\bar{v}\Delta t$ should be greater than the pore diameter D_p. Otherwise, the gas molecule's traveling trajectory *before* entering the pore mouth region is not recorded, because the entering event occurred longer than Δt ago, and we lose the information about whether the gas molecule comes from the bulk gas or from the surface adsorption layer. Second, $\bar{v}\Delta t$ should be less than the gas mean free path λ to ensure that gas–gas collisions do not confound the angle of incidence distribution. Accordingly, the following inequality should be satisfied by $\overline{v}\Delta t$: $D_p < \overline{v}\Delta t < \lambda$. According to the Maxwell-Boltzmann distribution, $\overline{v} = \sqrt{\frac{8k_BT}{\pi m}}$.[32] The gas mean free path is given by $\lambda = (\sqrt{2}\pi D_m^2 \rho)^{-1}$, where ρ is the volumetric number density of the bulk gas.[32] Consider one of the simulation cases for CO_2, where the gas pressure is 7.4 bar, the temperature is 300 K, and the pore diameter is 3.9 nm. In this case, Δt should satisfy 10 ps $< \Delta t <$ 30 ps. For the two other gases and the two other pore sizes considered in this work, the upper and lower bounds for Δt may differ, and the corresponding Δt value can be carefully chosen in order to carry out a similar analysis as shown below.

Figure 7(b) shows the angle of incidence distribution corresponding to the abovementioned simulation case. The y axis represents the number of occurrences during the 5 ns simulation for each bin of the angle of incidence on the x axis. When Δt = 1.2 ps, only a very short length of the molecular trajectory close to the pore mouth is recorded, and the angle of incidence follows the distribution $f \propto \sin\theta\cos\theta$ (top panel in Fig. 7(b)), indicating an entirely random angular distribution.[7] In other words, this distribution shows no memory regarding the pore. As the time interval Δt increases, a peak at high angle of incidence emerges, reflecting the contribution from the surface adsorption layer. At a time interval of 16 ps, the angle of incidence distribution exhibits both a broad direct impingement peak at 45° and a sharp surface diffusion peak at near 90° (second to bottom panel in Fig. 7(b)). As Δt is further increased to 40 ps, which is higher than the upper limit of 30 ps determined by the relation $\overline{v}\Delta t < \lambda$, the direct impingement peak becomes biased as it shifts to the low angle of incidence direction, due to gas–gas collisions (bottom panel in Fig. 7(b)). Considering that Δt should satisfy the constraint, 10 ps $< \Delta t <$ 30 ps, for CO_2 for a pore with D_p equal to 3.9 nm, we choose Δt = 16 ps as the most appropriate choice for later analysis (top panel in Fig. 7(c)).

Using the above-mentioned methodology, we can analyze the angle of incidence distribution of the permeation events which were previously classified into the surface diffusion or the direct impingement pathways. Note that we determined the pathway of a permeation event by examining whether the gas molecule entered the pore mouth region from the top or from the side. As shown in the middle panel in Fig. 7(c), the angle of incidence distribution corresponding to the surface diffusion pathway shows a single peak at high angle, because the trajectories of the surface diffusion pathway are parallel to the graphene plane and perpendicular to the z direction. On the other hand, as shown in the bottom panel in Fig. 7(c), the angle of incidence distribution corresponding to a direct impingement pathway exhibits a minor peak at high angle, along with a broad sinθcosθ peak at 45° associated with random impingement. This minor peak indicates that a fraction of the direct impingement events originated from the surface adsorption layer (Fig. 7(a)), and therefore, could not be predicted by our original bulk-gas-based theory (Eq. (21)). This additional minor pathway explains well the surplus of MD simulation-observed direct impingement attempts over those predicted by our original theory.

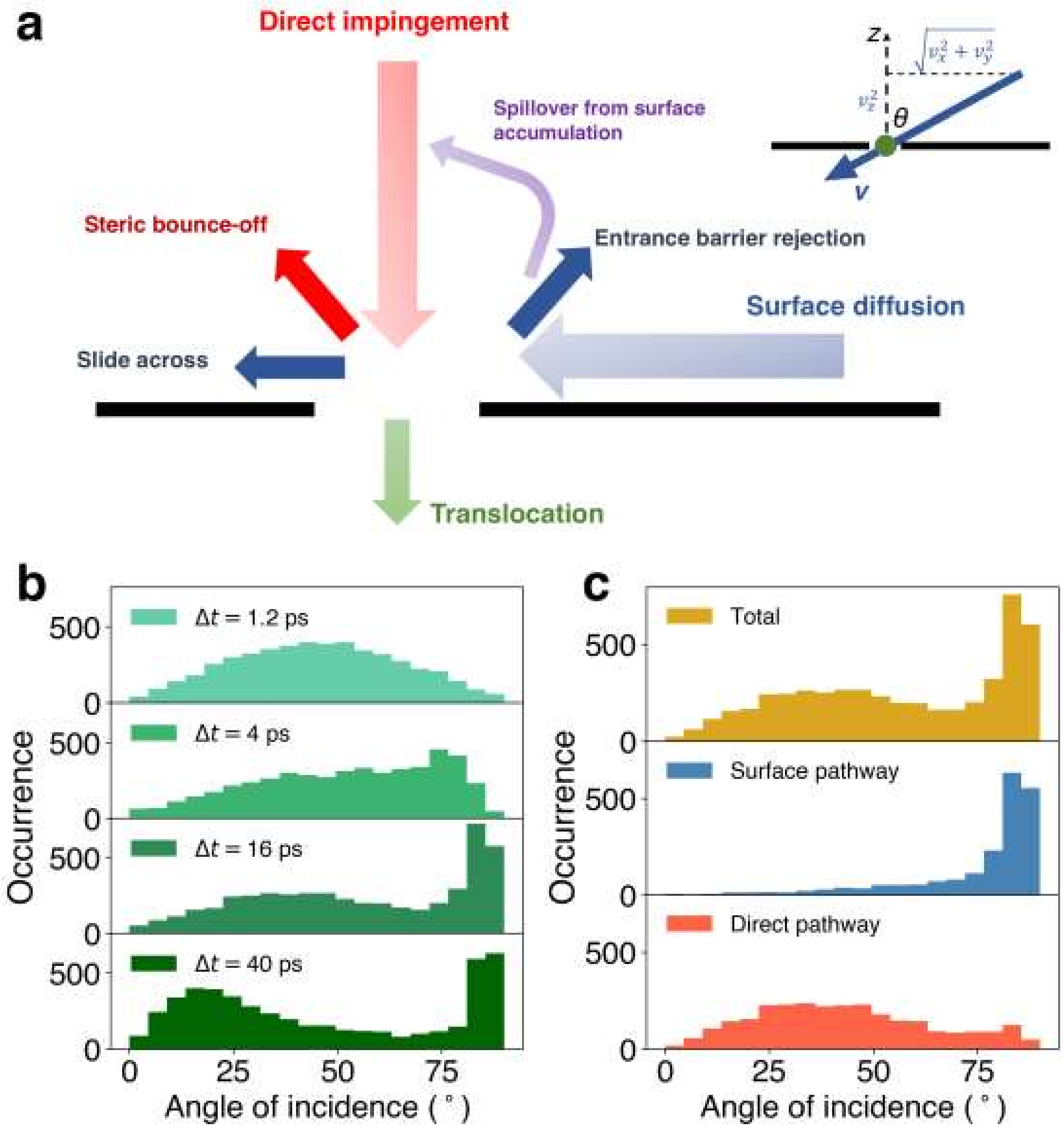

Figure 7: (a) Schematic illustration of the gas permeation mechanism through a graphene nanopore. (b) Angle of incidence distribution of a CO_2 molecule crossing a 3.9-nm-diameter graphene pore with Δt ranging from 1.2 ps to 40 ps. (c) Angle of incidence distribution of a CO_2 molecule crossing a 3.9-nm-diameter pore from the direct impingement and the surface diffusion pathways, where Δt

= 16 ps. The minor peak at high angle of incidence in the direct impingement pathway represents a minor spillover pathway.

Figure 7(a) illustrates this additional minor pathway as a spillover resulting from surface accumulation (the purple arrow). As shown previously, the majority of the surface injection attempts into the pore area are rejected (the blue arrows). These rejected gas molecules create a local high gas density in the vicinity of the pore, and get recirculated as direct impingement (the red arrow). Therefore, the minor spillover pathway possesses characteristics of both the direct and the surface pathways, which motivates the following power law estimation:

$$K_{\text{minor}} = aK_{1,\text{theory}}^{b}K_{2,\text{theory}}^{c} \tag{29}$$

where a, b, and c are fitting parameters, and $K_{1,\text{theory}}$ and $K_{2,\text{theory}}$ are the theory-predicted permeances per pore corresponding to the direct impingement (Eq. (21)) and the surface diffusion pathways (Eq. (22)), respectively. The fitted results for CO_2, CH_4, and Ar at different temperatures are: $a = 2.76 \times 10^{-3}$, $b = 0.31$, and $c = 0.91$ ($R^2 = 0.88$, Fig. S8). The unit for the permeances per pore appearing in Eq. (29) is molecule Pa^{-1} s^{-1}. Because $c > b$, the minor spillover pathway depends more strongly on the surface diffusion pathway, and demonstrates a pore size dependence of $(D_p^2)^{0.31}(D_p)^{0.91} = (D_p)^{1.53}$.

Combining Eqs. (20) to (29), when the translocation resistance is negligible, the predicted permeance per graphene nanopore is given by:

$$K = \delta K_{1,\text{theory}} + \gamma_{\text{inj}}\gamma_{\text{trans}}K_{2,\text{theory}} + 2.76 \times 10^{-3}K_{1,\text{theory}}^{0.31}K_{2,\text{theory}}^{0.91} \tag{30}$$

Note that the gas permeance contribution from the minor spillover pathway (the third term on the right hand side of Eq. (30)) is orders of magnitude smaller than the contributions from the direct impingement pathway (the $\delta K_{1,\text{theory}}$ term in Eq. (30)) and the surface diffusion pathway (the $\gamma_{\text{inj}}\gamma_{\text{trans}}K_{2,\text{theory}}$ term in Eq. (30)). Accordingly, in the following discussions regarding gas permeation through graphene nanopores, it is safe to neglect the spillover pathway. Note that, for other 2D materials, other pore sizes/densities, or other gases, the value of a in Eq. (29) may be non-negligible, and the spillover pathway should be considered. In the current case of graphene, we can approximate $K \approx \delta K_{1,\text{theory}} + \gamma_{\text{inj}}\gamma_{\text{trans}}K_{2,\text{theory}}$. Comparing this equation with our theoretical model, $K = K_1 + K_2$ (Eq. (20)), we see that the gas permeances per pore from the direct impingement pathway and the surface diffusion pathway need to be corrected by three factors: δ, γ_{inj}, and γ_{trans}. We therefore insert these three correction factors into our original theoretical prediction in

Eq. (14), which includes the translocation step, and obtain the overall gas permeation resistance for a wider pore diameter range, including the activated (translocation-limited) regime. Specifically,

$$R = R_3 + \frac{1}{\frac{1}{R_1}+\frac{1}{R_2}} = \frac{1}{\delta k_1 + \gamma_{\text{inj}}\gamma_{\text{trans}}k_2 H_{\text{surf}}} + \frac{1}{k_{\text{trans}}H_{\text{pore}}} \quad (31)$$

It is noteworthy that our group has recently derived an expression for the transport resistance of the translocation step R_3 based on transition state theory and MD simulations.[19] Accordingly, we can combine all the relevant expressions, including using relevant numbers for the translocation ($k_{\text{trans}}H_{\text{pore}}$ in Eq. (31)), direct impingement (δk_1 in Eq. (31)), and surface diffusion ($\gamma_{\text{inj}}\gamma_{\text{trans}}k_2 H_{\text{surf}}$ in Eq. (31)) pathways to predict the gas permeance per pore for graphene pores ranging from 0.5 to 6 nm in diameter for CO_2 (Fig. 8, Fig. S9(c)), CH_4 (Fig. S9(a)), and Ar (Fig. S9(b)). Because we do not have exact mathematical expressions to predict γ_{inj} and γ_{trans}, some approximations need to be made to estimate their values for other pore diameters. In order to calculate γ_{inj}, $E_{a,\text{inj}}$ needs to be first obtained using Eq. (26). To this end, we observed that $E_{a,\text{inj}}/|\Delta H_{\text{ads}}| = 0.25$, as seen from the empirical relation between the two energetic terms (Table 1). It is noteworthy that the value of $E_{a,\text{inj}}/|\Delta H_{\text{ads}}|$ could change as a function of pore functionalization. For example, oxygen termination would attract CO_2 molecules into the pore due to stronger electrostatic and dispersion interactions, thereby reducing $E_{a,\text{inj}}$. In the case of γ_{trans}, the values of γ_{trans} are estimated by linear interpolation of our MD simulation results. Note that we assume that our predictions of the correction factors, δ, γ_{inj}, and γ_{trans}, can be extrapolated to the small pore limit. However, the exact values of the three correction factors in the small pore limit, corresponding to the activated gas transport, are difficult to obtain because their respective effects will be obscured by the rejections from the energy barrier for translocation.

Figure 8(a) shows the various contributions to the permeance per pore for CO_2 permeating through a circular pore of diameter ranging between 0.5 to 6 nm at 300 K, predicted using Eq. (31). The translocation (R_3^{-1}), direct impingement pathway (R_1^{-1}), and surface diffusion pathway (R_2^{-1}) transport kinetics scale differently with the pore diameter. For pores with $D_p < 0.72$ nm, the energy barriers associated with crossing the pore are greater than 2 kJ mol^{-1}, which impedes the translocation step. In this regime, the translocation step (solid green curve in Fig. 8(a), taken from our recent publication[16]) is slower than the surface diffusion step (blue curve in Fig. 8(a)): $R_3^{-1} < 1.4 \times 10^4\ \text{Pa}^{-1}\ \text{s}^{-1} < R_2^{-1}$. The critical transition pore diameter D_p^* can be calculated by equating the translocation and the surface pathway resistances:

$$k_{\text{trans}}(D_p^*)H_{\text{pore}} = R_3^{-1} = R_2^{-1} = \gamma_{\text{inj}}\gamma_{\text{trans}}(D_p^*)k_2(D_p^*)H_{\text{surf}} \quad (32)$$

According to Eq. (31), R_3 dominates the overall gas permeation (dashed black curve in Fig. 8(a)) in this translocation-dominated regime (see the overlap of the green and black curves), in accordance with the activated regime discussed in the Introduction Section. Note that in this regime, the direct impingement step (red curve in Fig. 8(a)) is much slower than the surface diffusion step (blue curve), and does not contribute much to the overall gas permeance. As the pore diameter increases beyond 0.72 nm, the energy barrier decreases to 0, and the translocation rate increases rapidly. This rapid increase is shown in Fig. 8(a) by the green dashed line extended out from the green solid curve as an estimated trend. When $D_p > 0.72$ nm, R_3^{-1} is greater than both R_1^{-1} and R_2^{-1}, and becomes increasingly less important in dictating the overall permeance per pore (Eq. (31)). As shown in Fig. 8(a), the overall permeance per pore (dashed black curve) makes a transition from the translocation dominated (solid green curve) to the surface diffusion dominated (blue curve) from $D_p = 0.72$ nm to 1 nm. For 1 nm $< D_p <$ 2 nm, the surface diffusion pathway dominates the overall permeance per pore, as shown by the close correlation of the dashed black curve and the blue curve between the two grey dashed lines in Fig. 8(a). Another regime transition occurs at $D_p^* = 3.4$ nm, where the direct impingement step (red curve) and the surface diffusion step (blue curve) have the same rates: $\delta(D_p^*)k_1(D_p^*) = R_1^{-1} = R_2^{-1} = \gamma_{\text{inj}}\gamma_{\text{trans}}(D_p^*)k_2(D_p^*)H_{\text{surf}}$. For a graphene pore larger than 4 nm in diameter, the direct impingement pathway dominates, which is consistent with the steric regime proposed by Wang *et al.*[26] The three regimes are separated by the two vertical grey dashed lines as shown in Fig. 8(a).

The cross-regime transition point for the graphene nanopore diameter depends on the permeating gas. The pore diameter at the transition point from the translocation-dominated regime to the surface diffusion pathway-dominated regime is more important because it is the upper limit of highly selective molecular sieving. As shown in Fig. S9(a) and (b), this transition pore diameter is 0.76 and 0.78 nm for CH_4 and Ar, respectively. This transition pore diameter is greater for larger gas molecules (CH_4, Ar), because for larger gas molecules, the translocation energy barrier remains significant for the graphene pores of larger sizes.

Our prediction indicates that the surface diffusion mechanism can dominate for a certain pore size range, albeit a relatively narrow one. It is worth noting that our simulations assume that the graphene surface is perfectly clean. However, experimentally, the graphene surface is susceptible to the adsorption of organic molecules from the gas phase, and polymer residues from the graphene transfer process.[37] These factors will likely reduce the surface pathway transport rate by decreasing the heat of adsorption or the in-plane diffusivity. Therefore, our work represents a potential upper bound for the surface diffusion pathway rate.

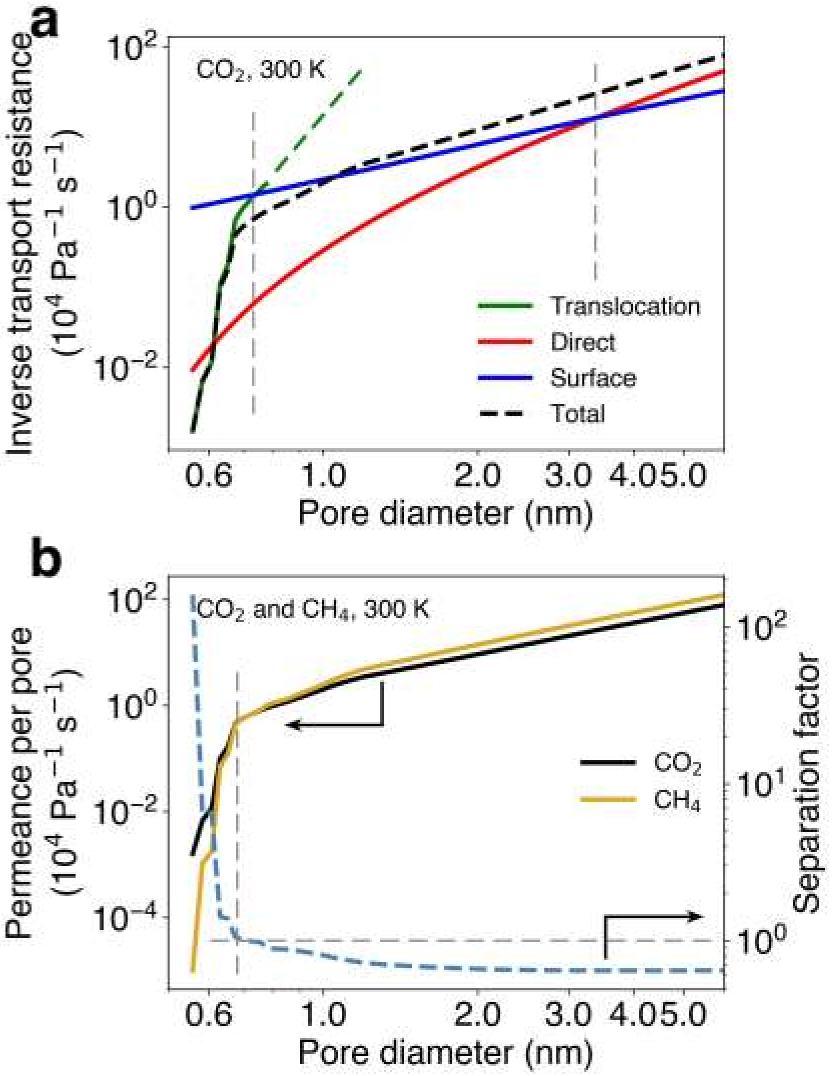

Figure 8: (a) Inverse transport resistances associated with the translocation (green), the direct impingement (red), and the surface diffusion (blue) pathways, and the overall permeance per pore (black) as a function of pore diameter for CO_2 at 300 K. The two perpendicular grey dashed lines separate three transport regimes, from left to right: translocation dominated, surface diffusion pathway dominated, and direct impingement pathway dominated, from left to right. (b) Permeance per pore of CO_2 and CH_4 (black and yellow curves, respectively) and corresponding CO_2/CH_4 separation factor (blue dotted curve) as a function of pore diameter at 300 K. The horizontal and perpendicular grey dashed lines denote the pore diameter value at which the values of the CO_2 and CH_4 permeances per pore are equal, and consequently, the separation factor is equal to 1.

By dividing the CO_2 permeance per pore in Fig. 8(a) by the CH_4 permeance per pore in Fig.

S9(a), we obtain the CO_2/CH_4 separation factor as a function of the pore diameter at 300 K (Fig. 8(b)). We are interested in this gas pair because CO_2/CH_4 separation is crucial in many industrial processes such as natural gas sweetening and oil recovery.[38] As shown in Fig. 8(b), a reasonable separation factor (> 5) can only be attained with a pore diameter less than 0.60 nm. This implies that Angstrom-scale precision is required in the nanopore fabrication process in order for the nanoporous graphene membrane to achieve a reasonably good CO_2/CH_4 separation performance.[39] We have also studied the effect of temperature (see Fig. S9(c)). The pore diameter restriction for CO_2/CH_4 separation is further tightened to 0.56 nm at 400 K (Fig. S9(d)), because a higher temperature attenuates the energy barrier difference between CO_2 and CH_4. At 300 K, the CO_2/CH_4 separation factor is 1 when D_p = 0.7 nm (Fig. 8(b)). This pore diameter is determined by a competition between the size and the mass of the gas molecules. On the one hand, CO_2 has a smaller gas kinetic diameter than CH_4, and therefore, has an edge over CH_4 when the pore size is small and the translocation step is dominant ($r_3 = k_{\mathrm{trans}} N_{\mathrm{pore}} \propto \exp(-E_a/k_B T)$). On the other hand, CH_4 has a smaller molecular weight and a higher average velocity. As a result, CH_4 gains the advantage in the large pore size limit where the surface diffusion and the direct impingement steps are dominant ($R_1^{-1} \propto m^{-\frac{1}{2}}$, and $R_2^{-1} \propto m^{-\frac{1}{2}}$, Eq. (21) and (22)). As D_p continues to increase, the direct impingement pathway dominates, and the separation factor approaches the Knudsen effusion selectivity limit ($K \propto m^{-1/2}$).

Conclusions

This paper presents a comprehensive theoretical framework to model gas permeation through graphene nanopores of any given diameter. Specifically, we derived analytical equations to predict the transport rates associated with the direct impingement and the surface diffusion steps, and then integrated them with the translocation step to formulate the overall gas permeation rate per pore. We showed that the transport resistances associated with the direct impingement and the surface diffusion steps are in parallel, and that the translocation step resistance is in series with the parallel combination. We then used molecular dynamics simulations to validate and refine the analytical model. Firstly, we showed that the direct impingement rate should be corrected by a success ratio δ. Secondly, we demonstrated that the surface diffusion rate to the pore should be corrected by two correction factors, γ_{inj} and γ_{trans}, characterizing the success ratio associated with diffusing into the pore area and crossing the pore, respectively. Finally, we identified a minor spillover pathway from the surface adsorption layer using an angle of incidence analysis. Based on these corrections, we predicted that the gas permeation through a graphene pore begins from a translocation-dominated regime, followed by a surface-pathway dominated regime, and finally by a direct-pathway dominated regime, as the pore diameter increases. Our modeling approach is applicable not only to nanopores in graphene, but also to nanopores in other two-dimensional materials, including hexagonal boron nitride and transition metal dichalcogenides (*e.g.*, molybdenum disulfide). Our work provides insights into the use of nanoporous 2D materials containing nanopores of varying sizes, for gas separation applications.

Methods

MD simulations were carried out using the large-scale atomic/molecular massively parallel simulator (LAMMPS).[40] The structures of the graphene pores are shown in Fig. 3(b)-(d). These pores are chosen to be circular because a circular pore shape is preferred during the etching of graphene.[41] Further, these pores are also considerably larger than the gas kinetic diameters because we focus on the non-activated transport regime, and need to avoid the effect of the energy barrier associated with crossing the pore. The diameter of the pore is defined as the in-plane distance between two opposing hydrogen atoms minus the van der Waals diameter of a hydrogen atom (0.22 nm).[42] The atoms in the porous graphene sheets were kept frozen during the simulation in order to clearly identify the positions of different regions (the bulk, the adsorption layer, and the pore mouth) with respect to the pore. Note that, in practice, graphene has out-of-plane thermal fluctuations of ~ 0.5 nm in amplitude and ~ 50 nm in wavelength,[43,44] corresponding to a tilting angle within 2°. Because the graphene pores in this study contain a large number of missing hexagons, we consider the thermal fluctuations as a minor perturbation, which should not affect the validity of our results. Even for small sub-nanometer graphene pores where thermal fluctuation effects should be more pronounced, freezing the motion of the carbon atoms in the graphene layer does not lead to a significant change in gas permeance.[19] Several gas molecules (200, 400, 600, or 1000) were evenly distributed in the two compartments and then allowed to diffuse through the nanopores. The simulated gases include CO_2, CH_4, and Ar. The simulations were carried out in the NVT ensemble using the Nose-Hoover thermostat with a time constant of 0.2 ps, within the temperature range of 300 K to 600 K.[45] The time step was 2 fs. The trajectories of all the gas molecules were recorded every 0.4 ps for a total simulation time of 5 ns.

All-atom force fields were used to describe the atomic interactions in the simulation, including bonded and non-bonded interactions. Bonded interactions include harmonic bonds and harmonic valence angles. The elementary physical model 2 (EPM2 model) was used for the stretching and the bending constants of CO_2,[46] and the all-atom-optimized potentials for liquid simulations (OPLS-AA model) was used for CH_4.[47] Non-bonded interactions include Lennard-Jones potentials and point-charge-based electrostatic potentials. We adopted the transferable potential for phase equilibria (TraPPE) force field[48] for the non-bonded interaction parameters of CO_2, and the OPLS-AA force field[47] for Ar. These force fields are able to reproduce the liquid-vapor equilibrium of the gas species, which is required in order to simulate the condensed adsorption phase on the graphene surface. The carbon atoms in the graphene lattice were modeled as uncharged atoms using the Lennard-Jones parameters reported by Cheng and Steele.[49] The carbon and the hydrogen atoms at the pore edge were modelled as charged, and their Lennard-Jones parameters and Coulombic partial charges were assigned values corresponding to the aromatic carbon (sp^2 carbon) in the AMBER force field.[50] The cutoff distance for the Lennard-Jones interactions was 1.2 nm. Long-range electrostatic interactions were treated using the Particle-Particle-Particle Mesh (PPPM) method.[51] Periodic boundary conditions were utilized in all directions. Geometric combining rules were implemented to describe the non-bonded interactions between different atoms.

Acknowledgement

This work used the Extreme Science and Engineering Discovery Environment (XSEDE),[52] which is supported by the National Science Foundation (NSF) grant number ACI-1548562. This work was supported by NSF under grant number CBET-1907716.

Supporting Information Available

Supporting Information is available free of charge on the ACS Publications website.

Section S1: adsorption isotherms of gases on graphene;

Section S2: velocity distribution of adsorbed gas on graphene;

Section S3: selection of the gas adsorption layer thickness on graphene;

Section S4: confidence interval calculation;

Section S5: details of the gas permeation analysis;

Section S6: fitting process for the minor spillover pathway;

Section S7: overall permeance prediction of other gases and temperatures.

References

(1) Liu, G.; Jin, W.; Xu, N. Two-Dimensional-Material Membranes: A New Family of High-Performance Separation Membranes. *Angew. Chem. Int. Ed.* **2016**, *55*, 13384–13397.

(2) Yoon, H. W.; Cho, Y. H.; Park, H. B. Graphene-Based Membranes: Status and Prospects. *Philos. Trans. R. Soc. Math. Phys. Eng. Sci.* **2016**, *374*, 20150024.

(3) Jiang, D.; Cooper, V. R.; Dai, S. Porous Graphene as the Ultimate Membrane for Gas Separation. *Nano Lett.* **2009**, *9*, 4019–4024.

(4) Liu, G.; Jin, W.; Xu, N. Graphene-Based Membranes. *Chem. Soc. Rev.* **2015**, *44*, 5016–5030.

(5) Boutilier, M. S. H.; Hadjiconstantinou, N. G.; Karnik, R. Knudsen Effusion through Polymer-Coated Three-Layer Porous Graphene Membranes. *Nanotechnology* **2017**, *28*, 184003.

(6) Boutilier, M. S. H.; Sun, C.; O'Hern, S. C.; Au, H.; Hadjiconstantinou, N. G.; Karnik, R. Implications of Permeation through Intrinsic Defects in Graphene on the Design of Defect-Tolerant Membranes for Gas Separation. *ACS Nano* **2014**, *8*, 841–849.

(7) Yuan, Z.; Benck, J. D.; Eatmon, Y.; Blankschtein, D.; Strano, M. S. Stable, Temperature-Dependent Gas Mixture Permeation and Separation through Suspended Nanoporous Single-Layer Graphene Membranes. *Nano Lett.* **2018**, *18*, 5057–5069.

(8) Surwade, S. P.; Smirnov, S. N.; Vlassiouk, I. V.; Unocic, R. R.; Veith, G. M.; Dai, S.; Mahurin, S. M. Water Desalination Using Nanoporous Single-Layer Graphene. *Nat. Nanotechnol.* **2015**, *10*, 459–464.

(9) Kazemi, A. S.; Hosseini, S. M.; Abdi, Y. Large Total Area Membrane of Suspended Single Layer Graphene for Water Desalination. *Desalination* **2018**, *451*, 160–171.

(10) Kidambi, P. R.; Boutilier, M. S. H.; Wang, L.; Jang, D.; Kim, J.; Karnik, R. Selective Nanoscale Mass Transport across Atomically Thin Single Crystalline Graphene Membranes. *Adv. Mater.* **2017**, 1605896.

(11) O'Hern, S. C.; Stewart, C. A.; Boutilier, M. S. H.; Idrobo, J.-C.; Bhaviripudi, S.; Das, S. K.; Kong, J.; Laoui, T.; Atieh, M.; Karnik, R. Selective Molecular Transport through Intrinsic Defects in a Single Layer of CVD Graphene. *ACS Nano* **2012**, *6*, 10130–10138.

(12) O'Hern, S. C.; Boutilier, M. S. H.; Idrobo, J.-C.; Song, Y.; Kong, J.; Laoui, T.; Atieh, M.; Karnik, R. Selective Ionic Transport through Tunable Subnanometer Pores in Single-Layer Graphene Membranes. *Nano Lett.* **2014**, *14*, 1234–1241.

(13) Rollings, R. C.; Kuan, A. T.; Golovchenko, J. A. Ion Selectivity of Graphene Nanopores. *Nat. Commun.* **2016**, *7*, 11408.

(14) Sholl, D. S.; Lively, R. P. Seven Chemical Separations to Change the World. *Nature* **2016**, *532*, 435–437.

(15) Bernardo, P.; Drioli, E.; Golemme, G. Membrane Gas Separation: A Review/State of the Art. *Ind. Eng. Chem. Res.* **2009**, *48*, 4638–4663.

(16) Baker, R. W. Future Directions of Membrane Gas Separation Technology. *Ind. Eng. Chem. Res.* **2002**, *41*, 1393–1411.

(17) Robeson, L. M. The Upper Bound Revisited. *J. Membr. Sci.* **2008**, *320*, 390–400.

(18) Blankenburg, S.; Bieri, M.; Fasel, R.; Müllen, K.; Pignedoli, C. A.; Passerone, D. Porous Graphene as an Atmospheric Nanofilter. *Small* **2010**, *6*, 2266–2271.

(19) Yuan, Z.; Rajan, A. G.; Misra, R. P.; Drahushuk, L. W.; Agrawal, K. V.; Strano, M. S.; Blankschtein, D. Mechanism and Prediction of Gas Permeation through Sub-Nanometer Graphene Pores: Comparison of Theory and Simulation. *ACS Nano* **2017**, *11*, 7974–7987.

(20) Baker, R. W. *Membrane Technology and Applications*, 2nd ed.; John Wiley & Sons Ltd,: Chichester, 2004.

(21) Koenig, S. P.; Wang, L.; Pellegrino, J.; Bunch, J. S. Selective Molecular Sieving through Porous Graphene. *Nat. Nanotechnol.* **2012**, *7*, 728–732.

(22) Boutilier, M. S. H.; Jang, D.; Idrobo, J.-C.; Kidambi, P. R.; Hadjiconstantinou, N. G.; Karnik, R. Molecular Sieving Across Centimeter-Scale Single-Layer Nanoporous Graphene Membranes. *ACS*

Nano **2017**, *11*, 5726–5736.
(23) Laidler, K. J.; Meiser, J. H. *Physical Chemistry*; Benjamin/Cummings Pub. Co: Menlo Park, 1982.
(24) Huang, S.; Dakhchoune, M.; Luo, W.; Oveisi, E.; He, G.; Rezaei, M.; Zhao, J.; Alexander, D. T. L.; Züttel, A.; Strano, M. S.; Agrawal, K. V. Single-Layer Graphene Membranes by Crack-Free Transfer for Gas Mixture Separation. *Nat. Commun.* **2018**, *9*, 2632.
(25) Drahushuk, L. W.; Strano, M. S. Mechanisms of Gas Permeation through Single Layer Graphene Membranes. *Langmuir* **2012**, *28*, 16671–16678.
(26) Wang, L.; Boutilier, M. S. H.; Kidambi, P. R.; Jang, D.; Hadjiconstantinou, N. G.; Karnik, R. Fundamental Transport Mechanisms, Fabrication and Potential Applications of Nanoporous Atomically Thin Membranes. *Nat. Nanotechnol.* **2017**, *12*, 509–522.
(27) Liu, H.; Dai, S.; Jiang, D. Insights into CO_2/N_2 Separation through Nanoporous Graphene from Molecular Dynamics. *Nanoscale* **2013**, *5*, 9984–9987.
(28) Tao, Y.; Xue, Q.; Liu, Z.; Shan, M.; Ling, C.; Wu, T.; Li, X. Tunable Hydrogen Separation in Porous Graphene Membrane: First-Principle and Molecular Dynamic Simulation. *ACS Appl. Mater. Interfaces* **2014**, *6*, 8048–8058.
(29) Du, H.; Li, J.; Zhang, J.; Su, G.; Li, X.; Zhao, Y. Separation of Hydrogen and Nitrogen Gases with Porous Graphene Membrane. *J. Phys. Chem. C* **2011**, *115*, 23261–23266.
(30) Sun, C.; Boutilier, M. S. H.; Au, H.; Poesio, P.; Bai, B.; Karnik, R.; Hadjiconstantinou, N. G. Mechanisms of Molecular Permeation through Nanoporous Graphene Membranes. *Langmuir* **2014**, *30*, 675–682.
(31) Sun, C.; Bai, B. Fast Mass Transport across Two-Dimensional Graphene Nanopores: Nonlinear Pressure-Dependent Gas Permeation Flux. *Chem. Eng. Sci.* **2017**, *165*, 186–191.
(32) Atkins, P.; De Paula, J. *Atkins' Physical Chemistry*, 8th ed.; Oxford University Press: New York, 2006.
(33) Brunauer, S.; Emmett, P. H.; Teller, E. Adsorption of Gases in Multimolecular Layers. *J. Am. Chem. Soc.* **1938**, *60*, 309–319.
(34) Fogler, H. S. *Elements of Chemical Reaction Engineering*, 5th ed.; Prentice Hall: Boston, 1999.
(35) Sun, C.; Bai, B. Gas Diffusion on Graphene Surfaces. *Phys. Chem. Chem. Phys.* **2017**, *19*, 3894–3902.
(36) Bell, I. H.; Wronski, J.; Quoilin, S.; Lemort, V. Pure and Pseudo-Pure Fluid Thermophysical Property Evaluation and the Open-Source Thermophysical Property Library CoolProp. *Ind. Eng. Chem. Res.* **2014**, *53*, 2498–2508.
(37) Lin, Y.-C.; Lu, C.-C.; Yeh, C.-H.; Jin, C.; Suenaga, K.; Chiu, P.-W. Graphene Annealing: How Clean Can It Be? *Nano Lett.* **2012**, *12*, 414–419.
(38) Zhang, Y.; Sunarso, J.; Liu, S.; Wang, R. Current Status and Development of Membranes for CO_2/CH_4 Separation: A Review. *Int. J. Greenh. Gas Control* **2013**, *12*, 84–107.
(39) Zhao, J.; He, G.; Huang, S.; Villalobos, L. F.; Dakhchoune, M.; Bassas, H.; Agrawal, K. V. Etching Gas-Sieving Nanopores in Single-Layer Graphene with an Angstrom Precision for High-Performance Gas Mixture Separation. *Sci. Adv.* **2019**, *5*, eaav1851.
(40) Plimpton, S. Fast Parallel Algorithms for Short-Range Molecular Dynamics. *J. Comput. Phys.* **1995**, *117*, 1–19.
(41) Rajan, A. G.; Silmore, K. S.; Swett, J.; Robertson, A. W.; Warner, J. H.; Blankschtein, D.; Strano, M. S. Addressing the Isomer Cataloguing Problem for Nanopores in Two-Dimensional Materials. *Nat. Mater.* **2019**, 18, 129–135.
(42) Rowland, R. S.; Taylor, R. Intermolecular Nonbonded Contact Distances in Organic Crystal Structures: Comparison with Distances Expected from van Der Waals Radii. *J. Phys. Chem.* **1996**, *100*, 7384–7391.
(43) Meyer, J. C.; Geim, A. K.; Katsnelson, M. I.; Novoselov, K. S.; Booth, T. J.; Roth, S. The Structure of Suspended Graphene Sheets. *Nature* **2007**, *446*, 60–63.
(44) Wang, W. L.; Bhandari, S.; Yi, W.; Bell, D. C.; Westervelt, R.; Kaxiras, E. Direct Imaging of Atomic-Scale Ripples in Few-Layer Graphene. *Nano Lett.* **2012**, *12*, 2278–2282.
(45) Hoover, W. G. Canonical Dynamics: Equilibrium Phase-Space Distributions. *Phys. Rev. A* **1985**, *31*, 1695.

(46) Harris, J. G.; Yung, K. H. Carbon Dioxide's Liquid-Vapor Coexistence Curve and Critical Properties as Predicted by a Simple Molecular Model. *J. Phys. Chem.* **1995**, *99*, 12021–12024.

(47) Jorgensen, W. L.; Maxwell, D. S.; Tirado-Rives, J. Development and Testing of the OPLS All-Atom Force Field on Conformational Energetics and Properties of Organic Liquids. *J. Am. Chem. Soc.* **1996**, *118*, 11225–11236.

(48) Potoff, J. J.; Siepmann, J. I. Vapor–Liquid Equilibria of Mixtures Containing Alkanes, Carbon Dioxide, and Nitrogen. *AIChE J.* **2001**, *47*, 1676–1682.

(49) Cheng, A.; Steele, W. A. Computer Simulation of Ammonia on Graphite. I. Low Temperature Structure of Monolayer and Bilayer Films. *J. Chem. Phys.* **1990**, *92*, 3858–3866.

(50) Cornell, W. D.; Cieplak, P.; Bayly, C. I.; Gould, I. R.; Merz, K. M.; Ferguson, D. M.; Spellmeyer, D. C.; Fox, T.; Caldwell, J. W.; Kollman, P. A. A Second Generation Force Field for the Simulation of Proteins, Nucleic Acids, and Organic Molecules. *J. Am. Chem. Soc.* **1995**, *117*, 5179–5197.

(51) Hockney, R. W.; Eastwood, J. W. *Computer Simulation Using Particles*; Taylor & Francis Group: New York, 1988.

(52) Towns, J.; Cockerill, T.; Dahan, M.; Foster, I.; Gaither, K.; Grimshaw, A.; Hazlewood, V.; Lathrop, S.; Lifka, D.; Peterson, G. D.; Roskies, R.; Scott, J. R.; Wilkins-Diehr, N. XSEDE: Accelerating Scientific Discovery. *Comput. Sci. Eng.* **2014**, *16*, 62–74.